# Aerodynamic Removal and Characterization of Particulate Trace Residues on Model Surfaces

Kalyan Kottapalli

A thesis

submitted in partial fulfillment of the

requirements for the degree of

Master of Science in Mechanical Engineering

University of Washington

2017

Committee:

Igor. V. Novosselov, Chair

Alexander V Mamishev

Alberto Aliseda

Ramulu Mamidala

Program Authorized to Offer Degree:

Mechanical Engineering

University of Washington

## Abstract

**Aerodynamic Removal and Characterization of Particulate Trace Residues on Model Surfaces**

Kalyan Kottapalli

Chair of the Supervisory Committee:
Dr. Igor. V. Novosselov
Department of Mechanical Engineering

Trace residues of illicit substances and biological contamination of the surfaces remain accessible for long times because of their volatility. Although the non-contact surface sampling has been demonstrated using state-of-the-art sampling/detection platforms, the resuspension rates and the forces acting a nonspherical particle in the surface boundary flow are not well understood. The effectiveness and the sampling throughput of trace residues detection can be greatly enhanced by integrating the analytical instrument with a properly-designed sampling system. Aerodynamic particle resuspension is a function of many parameters, such as particle size, morphology, material, humidity, and turbulence. This work presents morphological analysis and analysis of the removal rates of two different trace explosives residues in an aerodynamic flow cell as a function of particle size and flow velocity. Samples of *Trimethylenetrinitramine* (RDX) and *2,4,6- Trinitrotoluene* (TNT) are prepared by dry transfer method on the glass surface and interrogated under various

flow conditions. The samples are examined optically and binned by their apparent area. They are also visualized by Scanning Electron Microscopy and Optical Profilometry to compute the height of the sample. This method is also applied to size-controlled reference particles in 5-50-micron range, the particle size range chosen based on the typical size distribution associated with trace explosives found in fingerprints. The resuspension efficiency is calculated as a function of the particle size and compared with the trace explosive particles in the same size range. Removal efficiency is proportional to the height (critical dimension) and inversely proportional to the dimension in the plane of the substrate. The particle removal data from the flow cell experiment is compared with the Computational Fluid Dynamics (CFD) modeling to correlate the removal with the wall shear stress showing a direct correlation with the particle removal rates.

# TABLE OF CONTENTS

# List of Figures

# List of Tables

# ACKNOWLEDGEMENTS

The task I took at hand has come to fruition, and it would not have been possible without the support and guidance of several people.

I would like to express my sincere gratitude to my advisor Prof. Igor V. Novosselov for giving me an opportunity to learn and work under his guidance, for his patience, motivation, enthusiasm, and immense knowledge. I could not have imagined having a better advisor and mentor for my Master's study. I would like to thank Dr. Ramulu Mamidala, Dr. Alexander V Mamishev and Dr. Alberto Aliseda for giving their valuable time to serve on my thesis committee. I am thankful to my lab mates especially Patrick Fillingham, Jiayang He, Byron Ockerman, Xiaolin Zhan and Justin Davis for their help and advice during my research work.

Finally, I would like to thank my family for being a continuous support through every thick and thin and my friends for being like a family away from home.

This work was supported by the DHS Science and Technology Directorate, Homeland Security Advanced Research Projects Agency, Explosives Division, and UK Home Office; grant no. HSHQDC-15-C-B0033

# **Chapter 1.** Introduction

"There is no problem more difficult to solve than that created by ourselves."

- Felix Alba- Juez

The creativity of those that would do the civilized word harm is seemingly limitless. This fact has been true throughout history; today is no exception. While civilized people might have difficulty understanding their enemies' motivation, they can and must use their creativity to conceive adequate defenses proactively. The most recent alarming increase in number and violence of terrorist bombings has made the task of standoff detection of improvised explosive devices extremely urgent. There is a current need to improve security screening methods for explosive detection. For example, in airports, it is important to detect the presence of hidden explosives in luggage, to detect explosive residues on people's hands, and to detect explosives on the aircraft itself [1]. Explosive detection is also needed to monitor vehicle surfaces at security checkpoints, for screening individual people, and for screening mail [1, 2]. These detection methods obviously must sense trace explosive residues that are left by individuals handling explosives.

Conventional trace particle collection methods refer to the "swab test" where the interrogated surface is swabbed with swab material and analyzed by a bench top instrument. This contact sampling method is susceptible to significant variations sample collection efficiency as a function of surface properties, sampling procedure, and sampling region geometry. In a non-contact sampling, particles and vapors are liberated from the surface and collected onto an analysis substrate or analyzed in their

aerosol state. The method has several advantages with respect to the operation and collected repeatability; however, the optimization of particle removal and collection has not been adequately described in the literature.

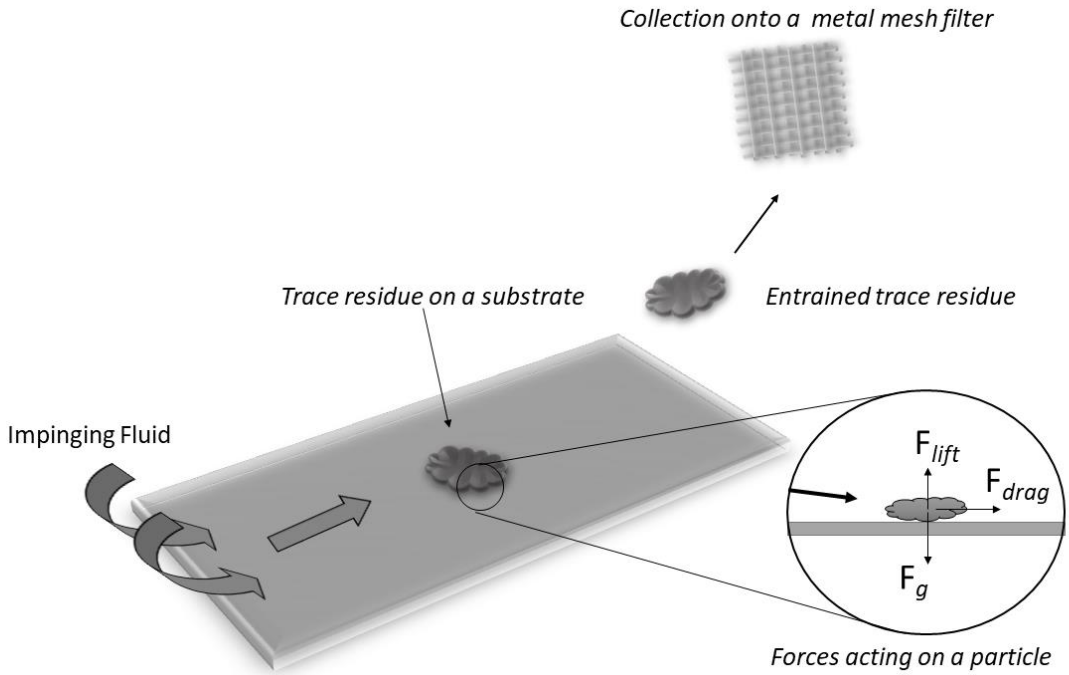


**Figure 1** *Aerodynamic particle resuspension: Particles and vapors are liberated from the surface and collected onto an analysis substrate or analyzed in their aerosol state.*

Several authors have shown the dependency of particle removal on the fluid properties of the flow in the vicinity of the particle[3-5]. Typically, controlled size microspheres are used as surrogates for explosive particles to study non-contact removal. In aerodynamic sampling where the particles are resuspended for the surface by a combination of lift and drag force acting on the particle in the boundary layer, the larger microspheres are resuspended at lower velocities than, the smaller ones [6]. Keedy et al. [3] compared resuspension of PSL microspheres and trace explosives particle in the aerodynamic removal scenario by varying the nozzle pressure and stand-off sampling distance. [7]. Several efforts describe the use of engineered particles for use as standards for trace explosives

particles for contact and non-contact sampling. Fletcher et al. (2008a) presented a methodology for fabricating polymer microspheres using inkjet printing of a biodegradable polymer containing high explosives for use as calibrants or verification standards for explosive trace detection. The use of polymer microspheres is advantageous because they are monodispersed, the sphere diameters can be tailored for specific tests, and the microspheres may contain high levels of the test compound [8]. For example, Phares et al. (2000c) studied the capture polystyrene spheres laced with 2,4,6-trinitrotoluene (TNT) using a translating gas jet setup. Pure TNT particles from a solution of toluene and TNT resulted in coarse and nonspherical particles; so, polystyrene was added to the solution to maintain particle sphericity [4]. Fletcher et al. (2008b) examined the removal of fluorescent polystyrene spheres by air jets from polycarbonate filters and muslin cloth surfaces. The bright yellow and green colour of the fluorescent polystyrene spheres made identifying them easily on the polycarbonate, and muslin cloth surfaces easy [6].

However, the scientific literature does not describe the effect of morphology on the resuspension of the trace residues. In this work, we develop a method to analyze the morphology of trace residues and evaluate the removal of surrogate and particulate trace residues by two methods. We analyze the removal in a controlled wall shear stress environment, i.e. aerodynamic flow cell is used to understand the major factors that affect the removal of trace residues. Secondly, trace residues are subjected to higher shear forces using an impinging jet setup. Removal of trace residues are related to the aerodynamic wall shear stress to compute the removal scenario as a function of particle size, $d_p$.

Though the scientific literature describes the removal scenario of trace explosives, it does not describe the collection of re-suspended trace explosives particles and vapors directly onto the analysis substrates. In this work to evaluate particle capture efficiency as a function of particle size, properties of the substrate, and operating conditions we use size controlled monodisperse silica particles. Glass

microspheres and other size controlled inert particles have been widely used to characterize the filtration/transmission efficiency in the literature e.g. [9] [10]. Some of the main benefits of using the glass microsphere over polystyrene spheres are their availability in the dry form (not in liquid suspension), wide size range, compatible with typical trace explosive residues, and compatibility with gravimetric analysis. The silica microspheres used in this work (8-100 micron) are similar in size with of the particulate matter found in the fingerprints of the trace explosive residues[7].

The aim of this investigation was to take a more integrated approach to understand the removal scenario of two different primary trace residues and compare it to the benchmark microspheres. The thesis describes a new approach to analyze the vertical dimension (height) of the trace residue to understand its impact on the aerodynamic entrainment under various conditions. This thesis is organized as follows: (i) Morphological characterization of trace residues using SEM and optical profilometry, (ii) The removal of trace residues and surrogates are analyzed in a controlled wall shear stress environment, (iii) Characterization of media for trace explosive collection and analysis.

# **Chapter 2.** Morphological Characterization of Particulate Trace Residues

## 2.1 Background

Characterization of particle shape has been historically performed by a variety of sizing techniques including sieving, settling, micro-metrically. Though these methods are still in use, automatic scanning devices with higher resolutions have enabled us to characterize the morphology particles and understand their implications on physiochemical processes. Conventionally, energetic particles have been visualized using 'top - down approach' which is essentially the use of benchtop microscope to evaluate the visible area at angled normal to the surface. This method cannot be used to characterize the contact area of the sample which is of critical importance while determining the removal scenarios. In this work, we compare the traditional top – down approach with angled scanning electron microscopy (SEM). Shape Factor parameter ($S_f$) is introduced to characterize the morphology as a function of the equivalent diameter of the particle. Optical profilometry is used to verify the vertical dimensions computed from the SEM.

## 2.2 Sample Preparation

Two primary trace explosives viz. RDX (Research Development Explosives) and TNT (2,4,6-Trinitrotoluene) are selected for the study for two main reasons: (a) they are easily available at trace concentrations and (b) are the primary ingredient of most of the tertiary explosives which are major detection targets at transit centers. RDX is the main energetic material usually used in common plastic explosives such as C-4, PE-4, and Semtex. TNT on the other hand primarily is used for mining purposes.

### 2.2.1 **Energetic Materials**

Chamberlain (2002) has outlined a procedure for preparing explosives for sampling, which we utilized in these experiments. The crystallized explosives sample prepared on a flexible Teflon strip are transferred onto the glass slides by rubbing the coupon back and forth several times against the surface as shown in Figure 2. This transfer is performed (as opposed to directly depositing the explosive solution onto the slide) in order to ensure repeatability of the particles structure[11]. The previous study[12] has suggested that if the explosive particles are wet-deposited onto the glass surface suggests that the particles would adhere more strongly in comparison to dry deposition. Furthermore, the transfer allowed the homogenous, condensed explosive to be broken up into smaller particles upon transfer.

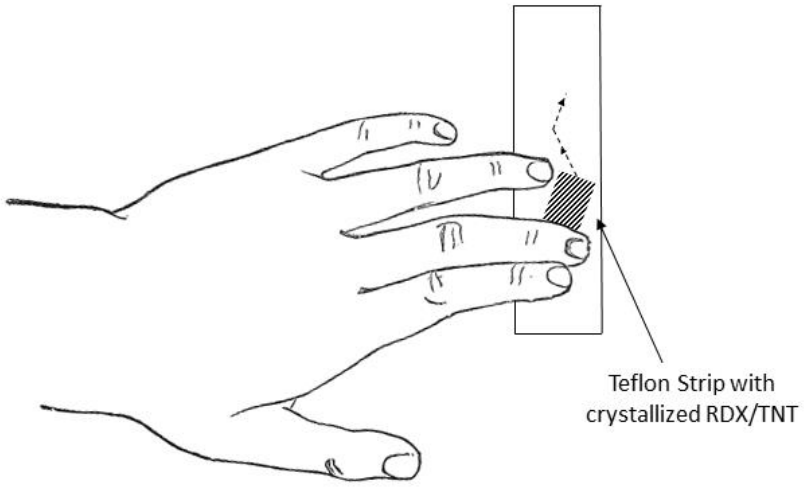


**Figure 2** *The dry deposition of trace residues of explosives from a Teflon® strip. The explosives are applied to glass slides by rubbing the coupon back and forth several times against the surface.*

The applied force during dry deposition affects the uniformity of the deposition. Fifty dry deposition experiments were conducted by measuring the force applied using a balance, and deposition

characteristics were studied. The previous study[13] shows that about 7.4 N of force is required to achieve a user independent uniform deposition. We found out that an average force of 7.2 N was needed to ensure a uniform dry deposition process.

A 1000 µg/mL solution of RDX in a 50/50 mixture of acetonitrile/methanol solvent (M83330-05, AccuStandard, Inc, New Haven, USA) was used to generate RDX crystals. A 10 µL drop of the standard solution was deposited on a 20 mm X 20mm Teflon Strip (300LSE, 3M, Inc., Maplewood, USA). Using this approach, large crystals of RDX were generated with a slow evaporation rate facilitated by the FEP on the Teflon strip. The Teflon strip is then stored in a desiccator for 24 hours before they are dry deposited onto the slide. Figure 3 (a) depicts the crystals formed on the Teflon strip. The crystals broke into smaller fragments (1 µm -50 µm) when dry deposited onto the glass slide. See Figure 3.(b).

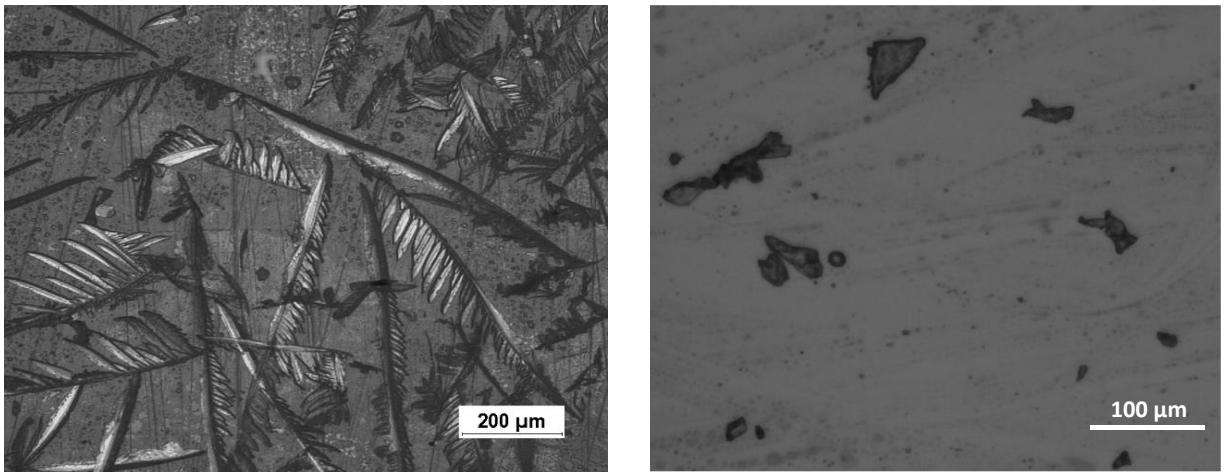


(a) (b)

**Figure 3** *The RDX solution was deposited on the Teflon strip and kept in the desiccator for 24 hours. (a) Typical crystal structure formed on the Teflon strip after 24 hours. (b) The crystals broke into smaller particles when dry deposited on the glass slide. The size distribution was quantified microscopically.*

TNT crystals are generated from a 1000 µL/mL solution of TNT in a 50/50 mixture of acetonitrile/methanol solvent (M-8330-11, AccuStandard, Inc, New Haven, USA). TNT when

deposited using the same method resulted in meta stable liquid droplets (*Figure 4 (a)*). TNT requires 7-8 times more time to form crystals when compared to the RDX [14]. TNT droplets require a nucleation site to form crystals. Previous researchers [15, 16] have used microspheres and water as a co-solvent to form TNT crystals. 10 μL drop of 1000 μL/mL solution of TNT was deposited on a small load of ceramic microspheres deposited using a glass capillary (02-688-115, Fisher Scientific, Inc, Waltham, USA). The ceramic microspheres form a nucleation site for the TNT liquid to form crystals on the Teflon strip. A batch of these strips were loaded and kept in the desiccator for 24 hours. During the dry transfer, these formed small particles of TNT on the glass substrate but had a few areas where metastable liquid glass form of TNT was also present. In addition to the latter problem, the microspheres were hard to distinguish from trace residues when visualized using a microscope.

A co-solvent method is preferable; it does not use the microspheres. A 10 μL drop of distilled water was added on top of the 10 μL drop of 1000 μL/mL solution of TNT. The acetonitrile and methanol evaporate at a much faster rate than water. Since TNT is insoluble in water, crystallization occurs on the interface as the solvents evaporate. The residual water evaporates over a 24 h period in the desiccator forming TNT crystals. These crystals are then dry deposited on the glass slide (*Figure 4 (b)*) and stored in the desiccator before being investigated in the experimental setups under various aerodynamic conditions.

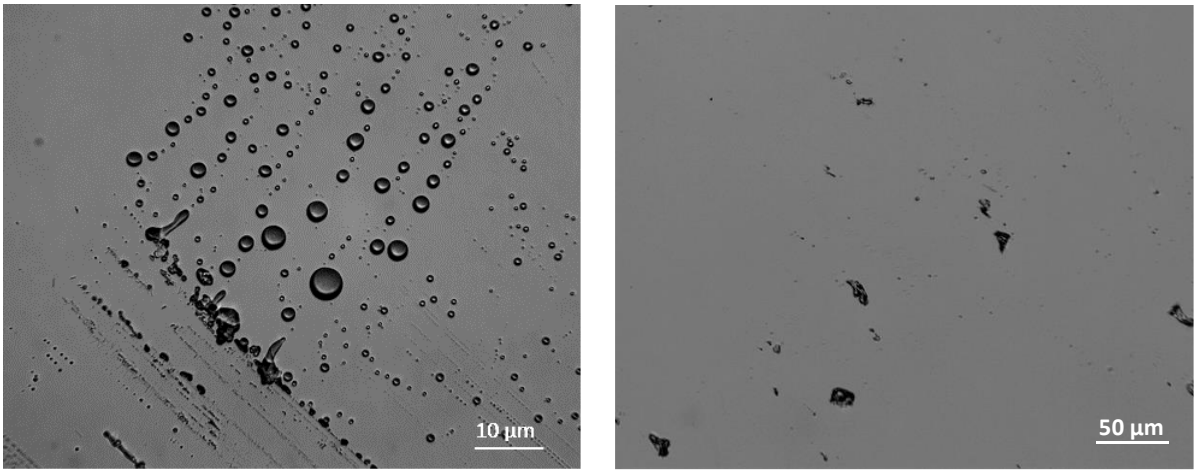


(a) (b)

**Figure 4** *The crystallization time for TNT is higher as compared to other energetic trace residues. (a) Metastable TNT droplets often present without assisted nucleation. (b) Nucleation sites are either generated by addition of ceramic microspheres or using the co-solvent method. The process is more controlled and repeatable with the co-solvent method.*

### 2.2.2 **Surrogate Particles**

The trace explosives particles in the fingerprints are of various sizes and morphology. In this study, monodispersed soda lime glass microspheres were used as surrogate particles. While the controlled size microspheres have often been used as surrogates, they do not possess the non-uniform morphological features of explosive particles. However, these surrogate particles are useful from a perspective of methods calibration and benchmarking of certain resuspension and collection parameters, as described later in the manuscript.

Polydispersed Soda Lime glass microspheres in 10 µm – 30 µm range (SLGMS-2.5 10-22 µm, Cospheric LLC, CA) are used in the morphological calibration experiments. Standard 25 mm x 75 mm microscope glass slides are used in the experiments, the slides pre-cleaned in an ultrasonic bath

and dried using compressed filtered dry air. The slides are then stored in the desiccator for 12 hours to ensure that all the moisture is removed. The microspheres are deposited gravitationally onto slides by dry nebulization. The dry nebulization is performed inside an aerosol chamber using a disposable aerosol vaporizer (HealthLine Corp., NY). Relative humidity in the chamber is controlled in the range of 30-40% to avoid the formation of capillary bridges at particle surface interface. The nebulization time is about 5 minutes before the vaporizer is turned off. During the nebulization, two computer fans (Thermaltake 20, Thermaltake USA Inc., CA) are used to maintain the recirculation flow inside the chamber during the process. This method provided the best particle deposition uniformity and is found to be very repeatable with minimal particle aggregation on the glass slides. The fans are shut down after 5 minutes, and an Aerodynamic Particle Sizer (TSI 3321, TSI Inc., Shoreview, MN, USA) is used to monitor the concentration of particles in the chamber.

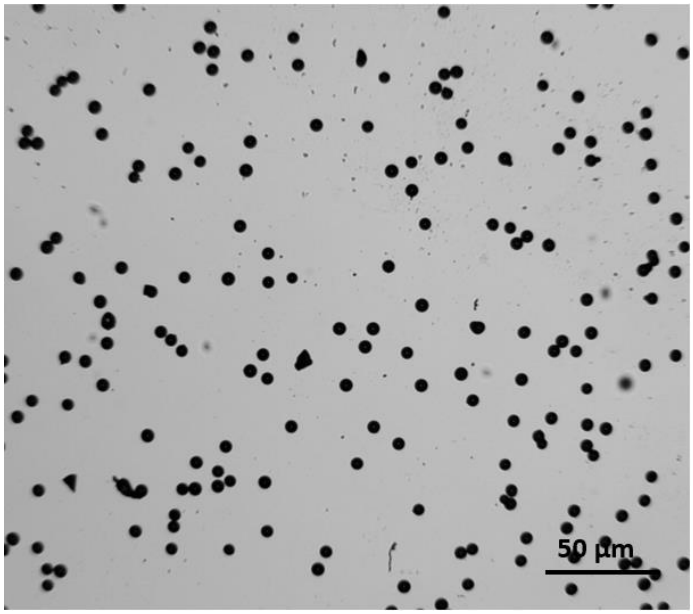


**Figure 5** *The Soda Lime glass microspheres are deposited onto the glass surface by dry nebulizing the particles in a controlled humidity chamber. The glass slides were stored in the desiccator for 24 hours before interrogation in the aerodynamic flow cell. A uniform distribution of surrogate particles was achieved.*

The target density is determined by two competing considerations related to particle resuspension experiments: (i) obtain high enough number density to achieve good statistics, (ii) the high loading may cause particle clumping, aerodynamic shadowing, and particle-particle interaction during the removal by rolling or sliding mechanisms.

## 2.3 Microscopic Characterization of Trace Residues

The removal efficiency of energetic particles (RDX and TNT) and surrogate (Soda lime glass microspheres) particles is evaluated microscopically by imaging the samples before and after exposure to various aerodynamic scenarios in the flow cell. The images are taken using Olympus BX 60 microscope fitted with a High-speed digital camera (OptixCam Summit D3K2). The Images are acquired at 14 MP resolution using ToupCam software. Only the leading edge of the particle deposition is evaluated, though it limits the number of total particles in the experiments, the rationale for this is two-fold: (i) avoiding ambiguity associated with particle relocation from upstream to downstream locations and (ii) reducing the probability of particle removal by contact, where the particle removed from upstream location travels along the surface (rolling, sliding or bouncing) and comes in a contact within the particle downstream location resulting in detachment of latter particle. In the case of energetic particles, a deposition area of 2 X 2 mm was scanned and stitched using an image analysis software. The stitched images are then preprocessed using MATLAB. For experiments where glass microspheres are used any non-circular elements (circularity <0.80) are removed before analysis using a microscopic images analysis software (Structure EN, iMicrotech Inc., NY, USA). The particle sizes are recorded and binned in sizes of 1 µm. The probability of size distribution for the samples is recorded and binned in sizes of 1 µm. The probability of size

distribution for the samples is calculated and plotted. Figure 6 shows the apparent size of the particle as seen at a normal angle to the substrate.

Since the soda lime microspheres were chosen in tight size ranges, they depict Poisson's distribution. Energetic particles, on the other hand, are dispersed randomly depicting binomial distribution with the majority of them in size range of 1μm -20 μm. Table 1 above discusses the average sizes and size range of the particles tested under various aerodynamic conditions in this study.

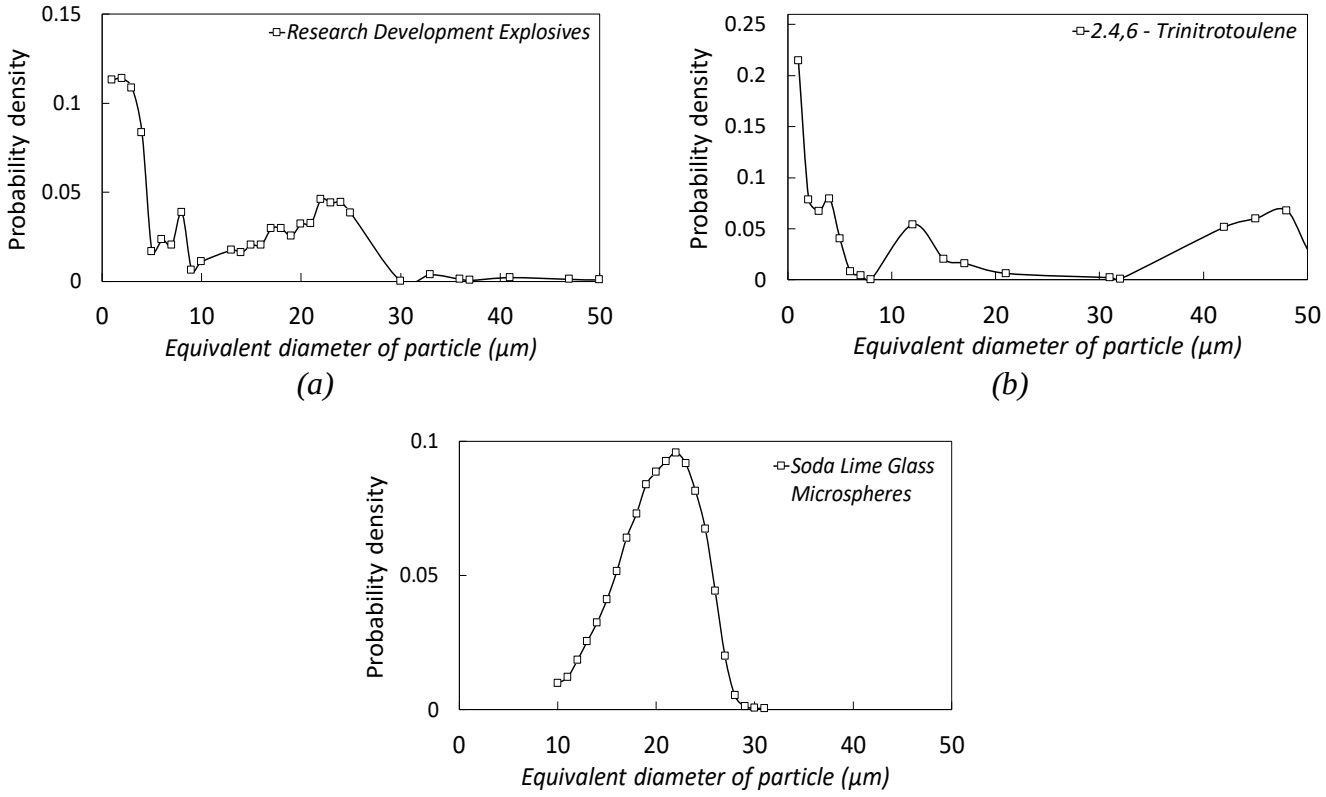


**Figure 6** *Probability of size distribution for energetic particles (RDX and TNT prepared by dry transfer) and surrogate particles (Soda Lime Glass microspheres) examined for testing in various scenarios in the aerodynamic flow cell. The energetic particles follow a binomial distribution while the surrogate particle follows a Poisson's distribution.*

**Table 1** *Average Equivalent diameter of various particles used for testing in the aerodynamic flow cell.*

| Material | Manufacturer | Average Equivalent Diameter (*μm*) |
|---|---|---|
| Soda Lime Glass Microspheres | Cospheric (SLGMS 10-22μm) | 19.68 ± 2.08 |
| Research Department Explosive | Accustandards (M-8330-05) | 14.35 ± 6.82 |
| 2,4,6-Trinirotoulene | Accustandards (M-8330-11) | 24.93 ± 12.02 |

## 2.4 Morphological Characterization of Trace Residues

The non-uniform structure of RDX and TNT particles present difficulties in the description of their geometries in typical modeling and simulation software. Various researchers [15, 17-21] have used atomic force microscopy (AFM) to study and evaluate the adhesion of various energetic materials. Though these studies provide valuable insight into the adhesion properties of different energetic materials like RDX, TNT, and PETN, they fail to provide us much insight into the morphology of the particle. Here the morphology is studied using two methods: (i) Scanning Electron Microscopy (SEM), and (ii) optical profilometry.

### 2.4.1 **Scanning Electron Microscopy**

With respect to aerodynamic particle resuspension, we hypothesized *that the frontal area, thus the height 'h' of the particle has a direct correlation with the resuspension rates*. Scanning electron microscopy (SEM) has been used traditionally to visualize the surface morphology. Recently, the SEM has been used to visualize the particle on surfaces for studies of particle removal efficiencies[22, 23]. To evaluate the morphology of the energetic material the RDX and TNT particles are deposited with controlled size microspheres for reference. They were used to evaluate the height 'h' of the samples. The SEM images are acquired using FEI Sirion XL30 (FEI, Hillsboro, OR).

The samples are prepared by the procedure described in Section 2.2.1. Microscopic Cover glass (#72230, EMS Inc., Hatfield, PA) is used as the substrate. The sample is sputter-coated with gold at 20 mA for 180 s before SEM observation to prevent charging of the specimen due to accumulating static charges. Figure 7 shows SEM images (without sputter) of the four different samples that have been used in this study.

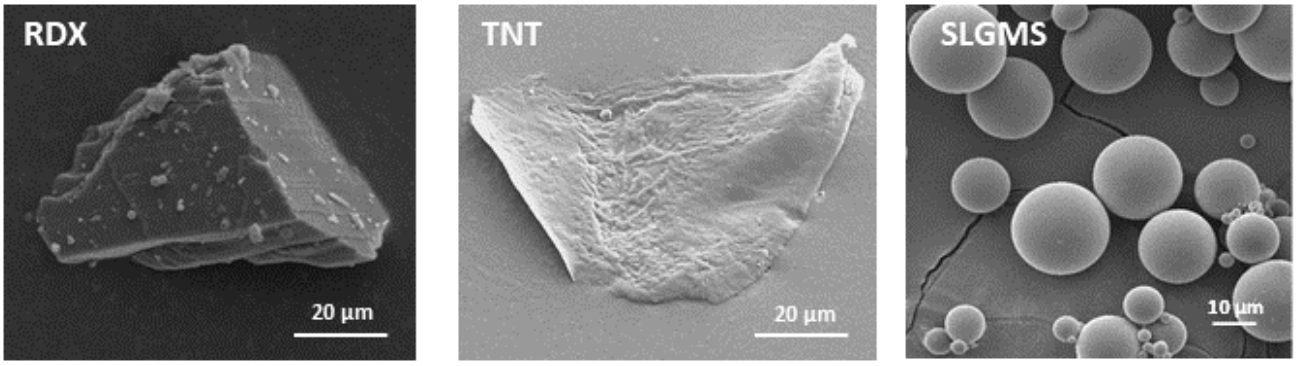


**Figure 7** *Scanning Electron Microscopic Images of RDX, TNT and Soda Lime Glass microspheres (SLGMS) respectively. The energetic materials formed particles of varied sizes and morphology when dry deposited on model surfaces like glass*

To determine the height of the sample, we develop a method that allows analyzing the particle size at several imaging angles. The particle size measurements are performed every 15 degrees (Figure 8), a 45-degree SEM pin mount on the Fei Sirion XL 30 was used to take images at angles up to 89 degrees from normal. At maximum tilt, due to the density of the particles on the glass slides only the particles at the outer edge could be visualized. For calibration particles were loaded at the corner of the slide.

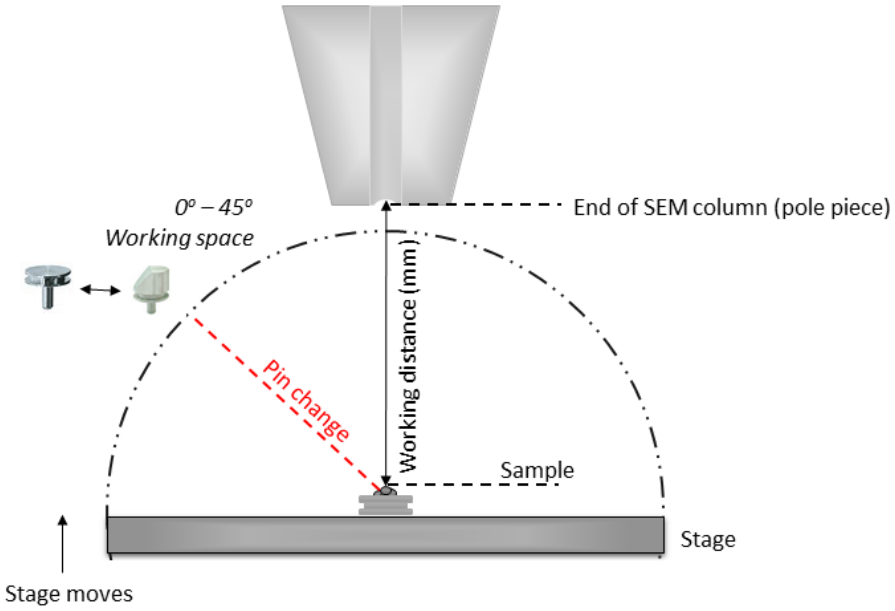


**Figure 8** *The SEM images are taken using two specimen holder pins: (a) standard Pin Ø12.7mm x 8mm, and, (b) Low profile 45º SEM Mount Ø12.7mm, short 6mm pin. The stage is moved from 0- 45 degrees to scan the sample from 0 to 90 degrees.*

As a reference, glass sphere (440345, Millipore Sigma, St; Louis, USA) of known size range (9-13 μm) are used. The size range chosen did not have any significance. It was one of the best precision spheres available in the market and hence were used for this study. This calibration process allows assessing the computational errors that could occur when trace residues will be examined using the same method. Figure 9 shows the SEM image of one of the glass spheres used a reference. The procedure s repeated 10 times to ensure repeatability of the results. The method yielded measurements which were in the ± 0.5 μm tolerance.

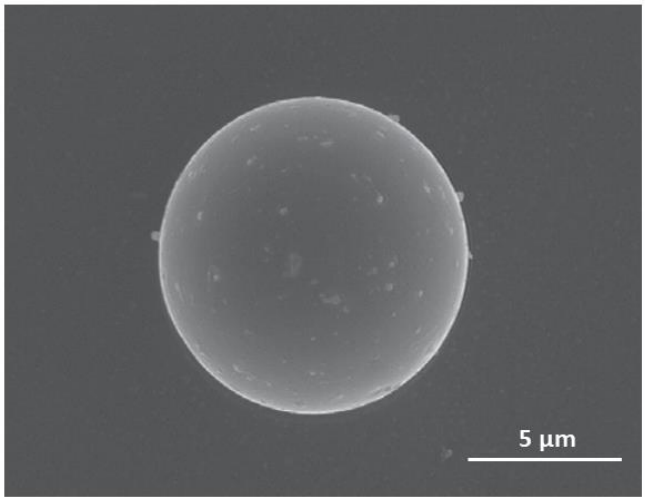


F**igure 9** *The SEM Images of glass spheres is used to calibrate the method of characterizing height from SEM images. The images were taken at tilt angles at every 15-degree interval.*

To evaluate the morphology of the RDX and TNT particles, 1 µg of RDX and TNT residue is deposited on the glass slide by dry deposition method as discussed in detail in section 2.2.1. Fifty individual particle height measurements are performed from twenty dry deposited samples for each material to obtain sufficient statistical data set. The particles are selected randomly in the deposited area to have the results independent of location. Figure 10 shows typical images taken at different tilt angles. These images are then processed by several MATLAB subroutines as described in the appendix. The input for MATLAB subroutine included the following parameters: tilt angle, the distance between the specimen surface, the final lens (working distance), and calibrated pixel size. The code does a pixel by pixel scan which is used to create a digital elevation model (DEM) for visualization particle morphology. Though detailed evaluation of particle morphology is feasible, in this study, we focused on a statistical approach to determine the maximum height and the shape factor of the particle. This information is critical to assess particle position in the boundary layer as discussed in detail in Section 3.4.

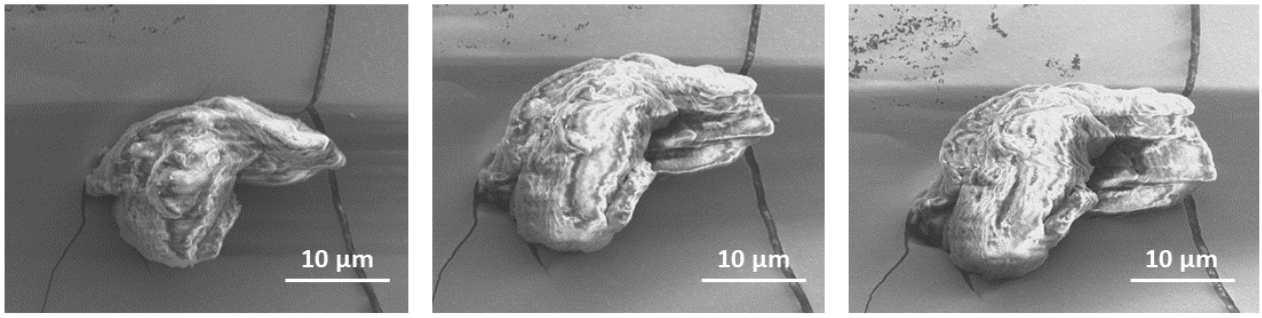


**Figure 10** *The SEM images of RDX particle on a glass slide was taken at 0, 30 and 45-degree tilt angle (left to right). The vertical dimension is then characterized by a set of algorithms which analyze the topology of the sample.*

The maximum particle height of RDX and TNT is computed, and data is represented in as a function of particle diameter shown in Figure 11. There is a logarithmic relation between the maximum height and diameter of the particle for TNT while the height for RDX was linearly dependent on the equivalent diameter. The empirical relations obtained from the fits represented in Figure 11 as shown in Table 2.

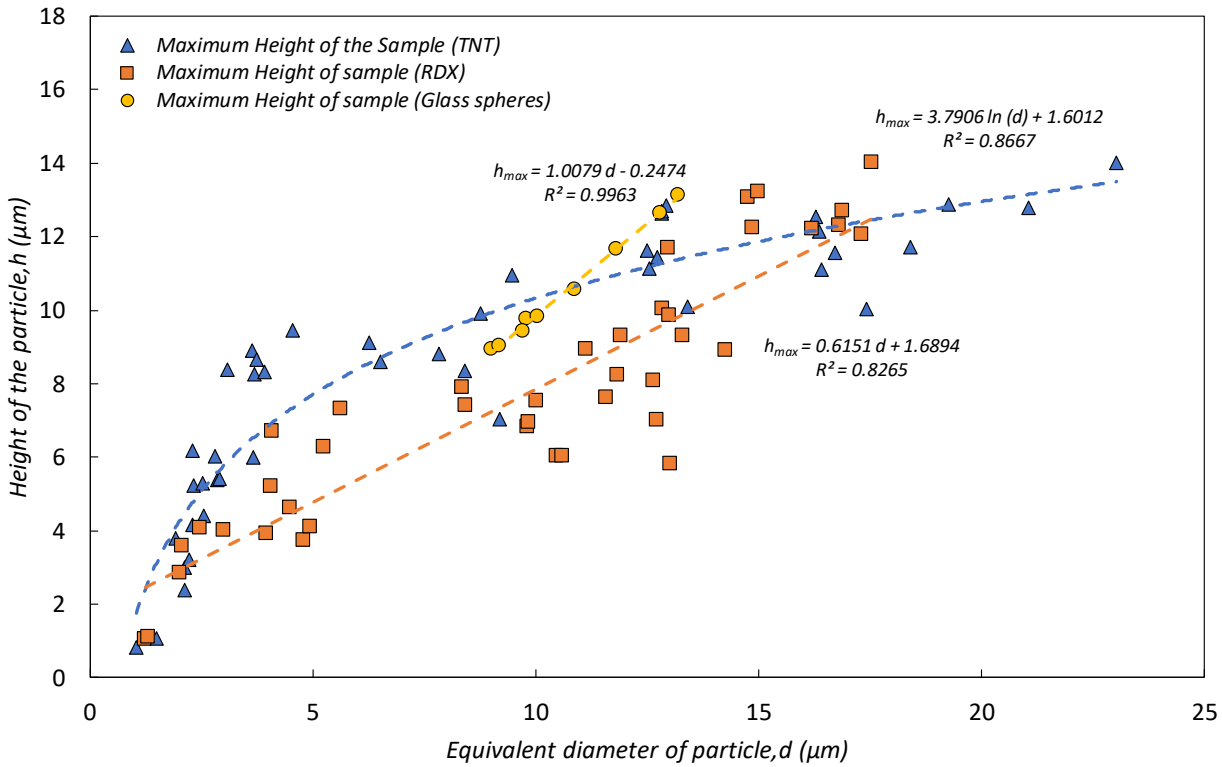


**Figure 11** *The Maximum height of the samples was computed from the SEM images using pixel density based algorithms.*

**Table 2** Relation between the maximum height and equivalent diameter of sample

| Material | Relation | R-Square value |
|---|---|---|
| Soda Lime Glass Microspheres | $h = 1.0079\,d - 0.2474$ | $R^2 = 0.9963$ |
| Research Department Explosive | $h = 0.6151\,d + 1.6894$ | $R^2 = 0.8265$ |
| 2,4,6-Trinitrotoluene | $h = 3.7906\ln(d) + 1.6012$ | $R^2 = 0.8667$ |

With respect to the calculation of forces and resulting moment acting on the particle, the position of the particle centroid is relevant. In our previous study[24], we characterized the forces acting on a soda lime glass microsphere on a glass surface. The rolling moment is calculated based on the calculated drag forces acting on a body and the position of the centroid.

For 3D shape, the centroid of the particle can be calculated by the two methods:

- Using calculus and the first-moment integral (*shown in Figure 12)*
- Using the method of composite parts and tables of centroids for average volumes.

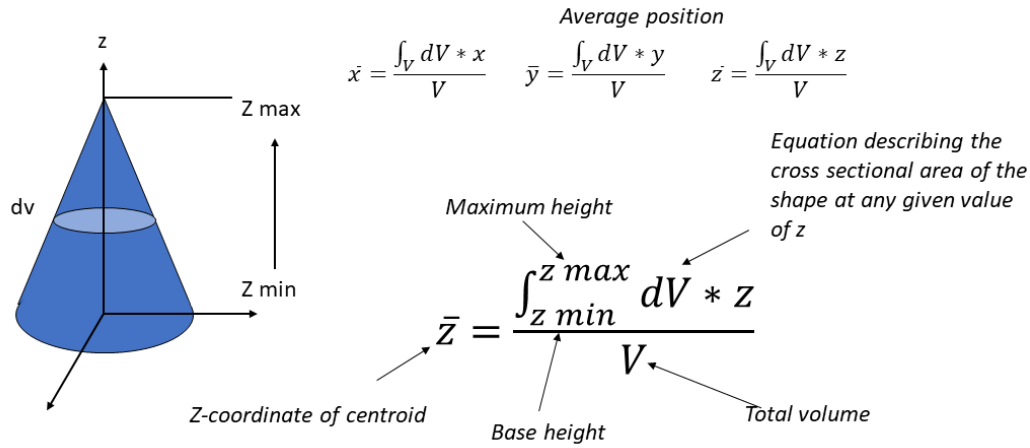


**Figure 12** *First moment integral method for calculation of centroid for a 3D Volume. The computation for a particle is time-consuming, and volumes at each cross section were hard to compute using images.*

The complex shape can be represented by an assembly of simple, well-defined shapes; the centroid for each shape can be determined. It is also possible to describe simple shapes mathematically. Centroid of the defined shapes is easier to compute than those of the complex shapes; however, combining these equations may become time-consuming in the case of complex shapes. Alternately, optical profilometry is used to determine the centroid height. The method maps the surface with a top-down approach and calculates the area in any plane of the particle morphology. The limitation of the method is that the void or gap information at the particle-surface interaction is not available.

### 2.4.2 **Optical Profilometry**

Optical profilers, including Keyence VK 9700, offer the unique ability to measure 3D profiles of any particle with a high vertical and lateral resolution. This method uses non-contact, scanning-confocal laser to generate quantitative 3D images. The microscope can measure profile heights (z) from 20 nm to 5 mm, and sub-micron x–y features rapidly and accurately. Pixel color changes determine the change in topography which is then simulated into height measurement data pixel by pixel. Figure 13 shows the example of RDX particle on a glass slide. We can observe two distinct types of particles.

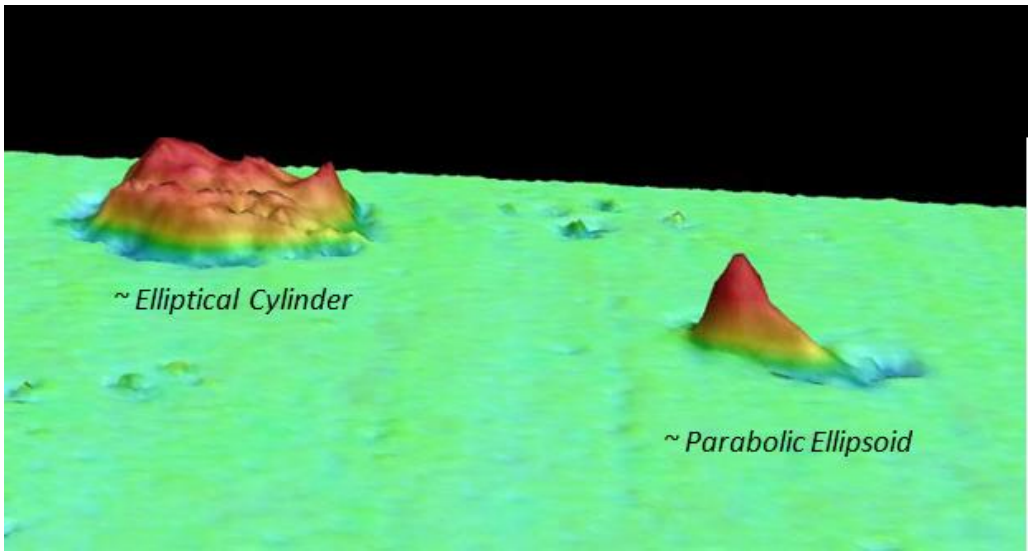


**Figure 13** *Screenshot of Profilometer results of RDX on a glass slide. The profilometer is based on a top down laser scan approach. It is only fit for measuring the maximum height and approximate centroid location.*

Laser Optical Profilometry is used to verify the results of angled SEM height measurements. Figure 14 plots the comparison between the values of the maximum height of the samples measured by both methods. The values agree closely with a tolerance of ± 0.5 μm.

Though the optical profilometer computes the height of complex morphological sample very accurately, it uses the top down approach and computes the particle-surface interface as a plane, overestimating particle contact area and underestimating the centroid height. From angled SEM

images, we know that the base of the sample has a curvature which is not taken account in the profilometer measurements. Potentially using the optical profilometer and angled SEM in parallel allows validating the SEM approach.

One of the key parameter, related to aerodynamic particle resuspension, is the comparison of the flow boundary layer thickness and the height of the particle. In particle adhesion force study[24], the CFD simulations of the flow over the surface provide the height of viscous sub layer (discussed in section 3.4) where the linear velocity can be used. Alternately, for some scenarios, the height of the boundary layer can be calculated based on the law of the wall assumptions.

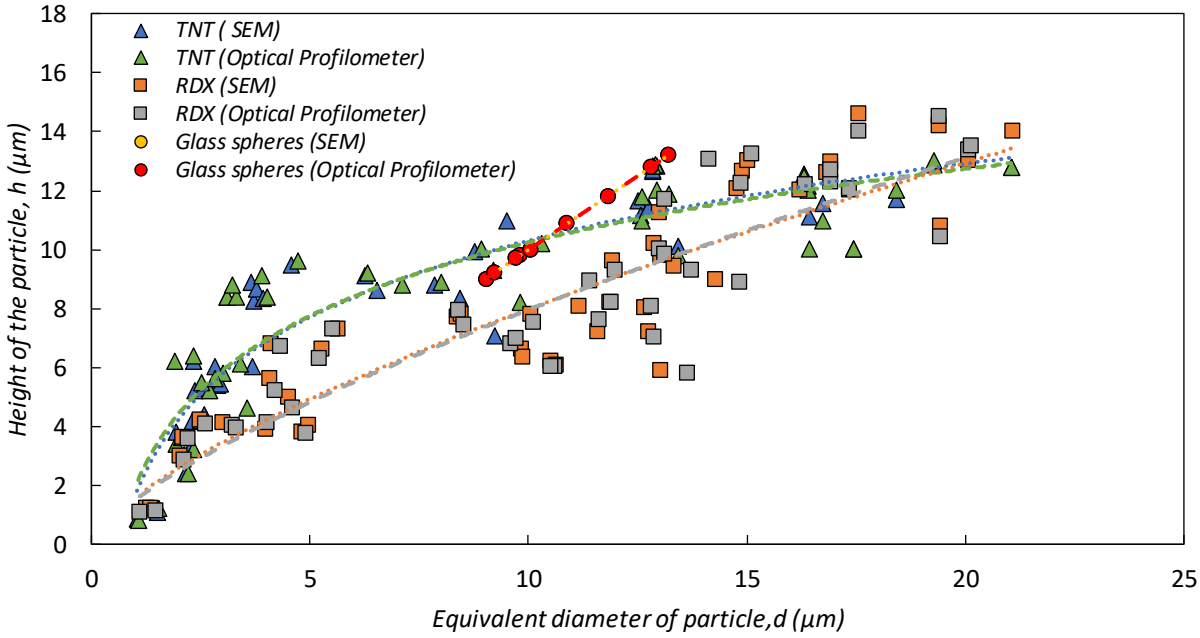


**Figure 14** *Comparison of maximum height measurements computed from Scanning Electron Microscopy and Optical Profilometry. The maximum height measurement from angled SEM and profilometer methods agree ± 0.5 µm.*

Figure 15 shows that as the particle diameter increases, the height of the sample reduces compared to the equivalent diameter in the x-y plane. In order to generalize the trends of the RDX depositions, the images are binned based on particle shape. Three morphologically similar sets are found as a function

of particle size (See Figure 15). The particle morphology changes from being parabolic to cylindrical. The particles with an equivalent diameter smaller than 20 μm have the aspect ratios closer to 0.5; these particles look like parabolic ellipsoids. The contact area is significantly larger than anticipated in most studies that have analyzed particle shape using microscopy at the perpendicular view. The empirical fit for the height of the RDX particle from the dry transfer is:

$$h_{max} = 3.5105 \ln(d) + 0.3567 \quad (1)$$

The empirical fit of the height of TNT particle from the dry transfer is:

$$h_{max} = 2.5662 \ln(d) - 3.4273 \quad (2)$$

The analysis of the particle height and centroid position suggests that for RDX particle prepared by a dry transfer procedure[11] from AccuStandard solutions, two distinct regions of particle shape can be identified:

*(i)* *Linear Region*

Particle height is directly proportional to its equivalent diameter in x-y plane; these particles are typically smaller than 20-25 micron in diameter, and

*(ii)* *Fixed Height Region*

Maximum particle height region where the equivalent diameter of the particle increases but the particle height remains the same, this height of the particle is nearly constant is in the range of 10-15 microns.

Figure 15 below shows the two different regions of particle shape as a function of equivalent diameter are discussed above. Three different types of morphology have also been shown pictographically represented in the plot.

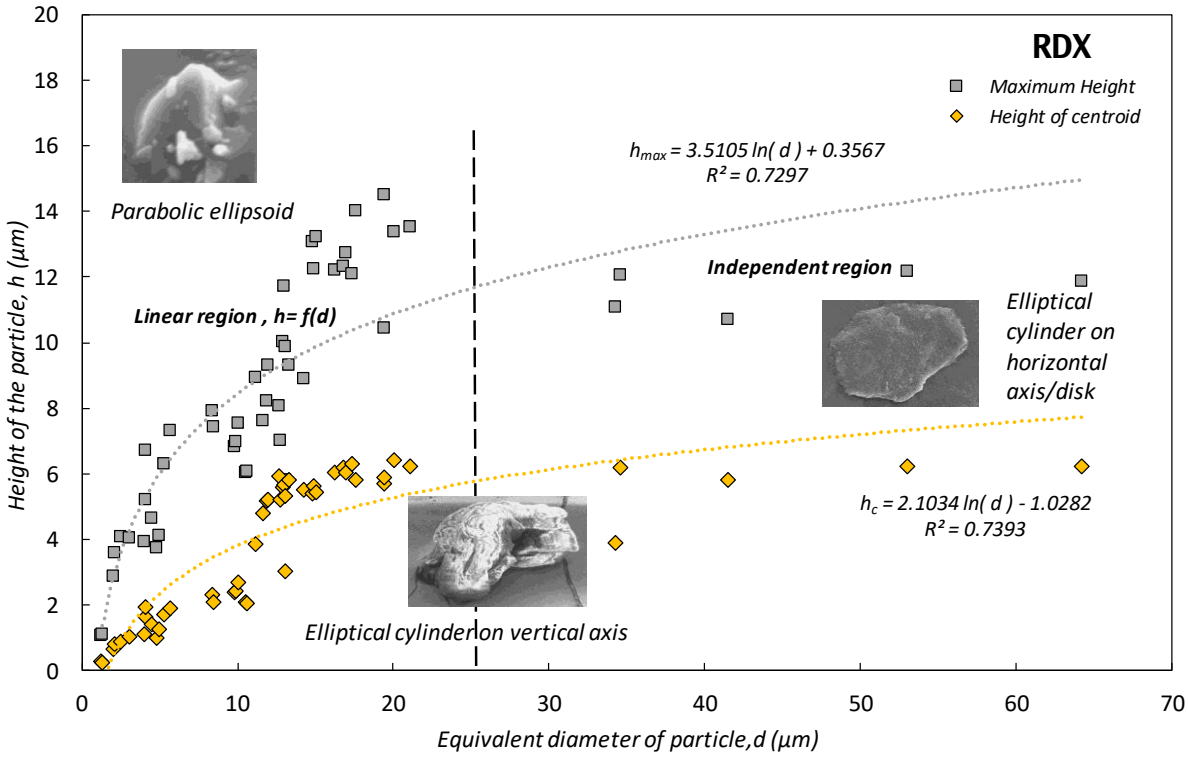


**Figure 15** *Maximum height and the height of centroid of RDX. The morphology was examined extensively, and we can bin the particles into three sets as a function of their equivalent diameter in the x-y plane. Centroid height computed using optical profilometer measurements.*

The majority of the particles are in the linear h =f (d) region. As we observe that the dry transfer method for deposition of RDX does not produce many particles with an equivalent diameter greater than 25 microns (Figure 6 and Figure 15), more precise fit can be found for these particles. Figure 16 shows the RDX particle analysis limited to 25-micron equivalent diameter. For this case, the empirical fit of the height of RDX particle.

For particles in the linear region,

$$h_{max}(d < 25\ \mu m):\ h_{max} = 0.5874\ d + 1.891 \tag{3}$$

$$h_c(d < 25\ \mu m): h_c = 0.3525\ d - 0.1115 \tag{4}$$

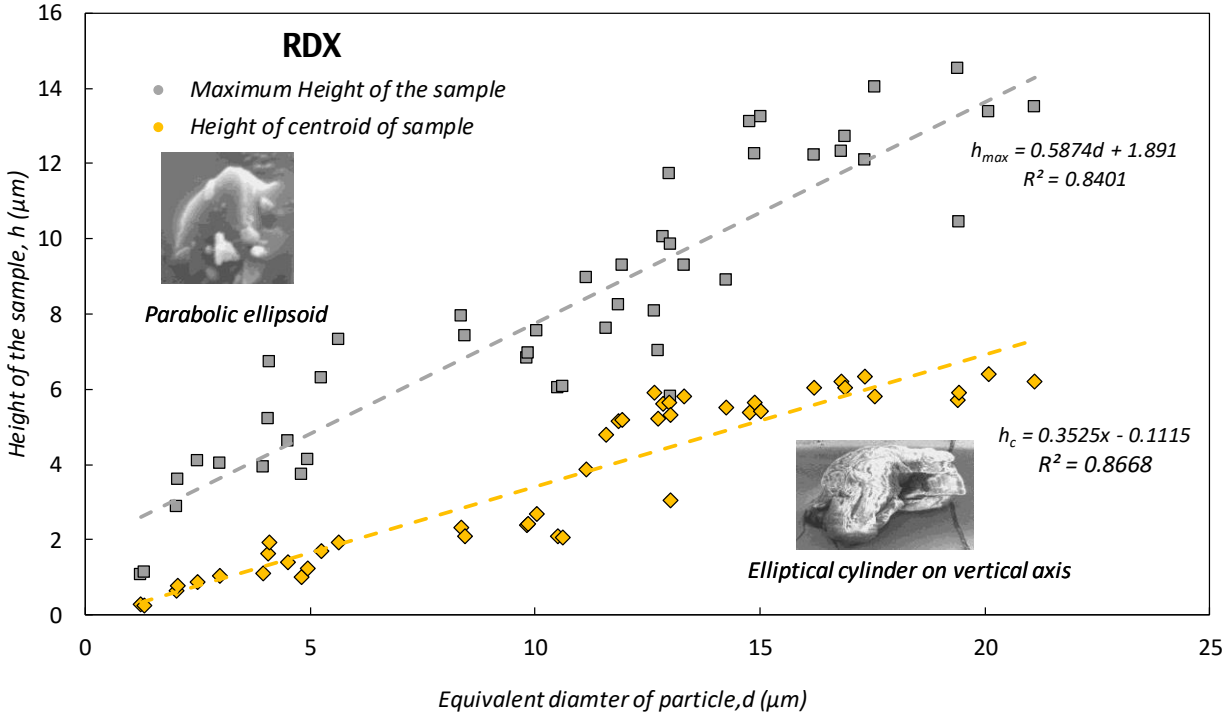


**Figure 16** *Maximum height and the height of centroid of RDX binned up to 25 μm. The maximum height of the sample and the height of centroid for RDX have a linear relation with the equivalent diameter of the particle. Centroid height computed using optical profilometer measurements.*

A similar analysis was done for 2,4,6 Trinitrotoluene (TNT). The TNT crystals are found to be thinner, and their maximum height was recorded at the raised edges. The analysis of the centroid position of these particles is more complicated. Figure 17 plots the maximum height and centroid height of the sample. The slope of the centroid location of the fit is smaller than the maximum height slope. This can be attributed to the error in profilometer technique as it includes the regions under the maximum height overestimating the particle volume. This would shift the centroid to be lower and

away from the center. As discussed previously the profilometer measurement are not likely to result in accurate estimates of the particle centroid.

The empirical fits for maximum height and height of centroid for a TNT particle are:

$$h_{max} = 2.5662\ \ln(d) - 3.4273 \tag{5}$$

$$h_c = 1.2671\ \ln(d) - 1.6405 \tag{6}$$

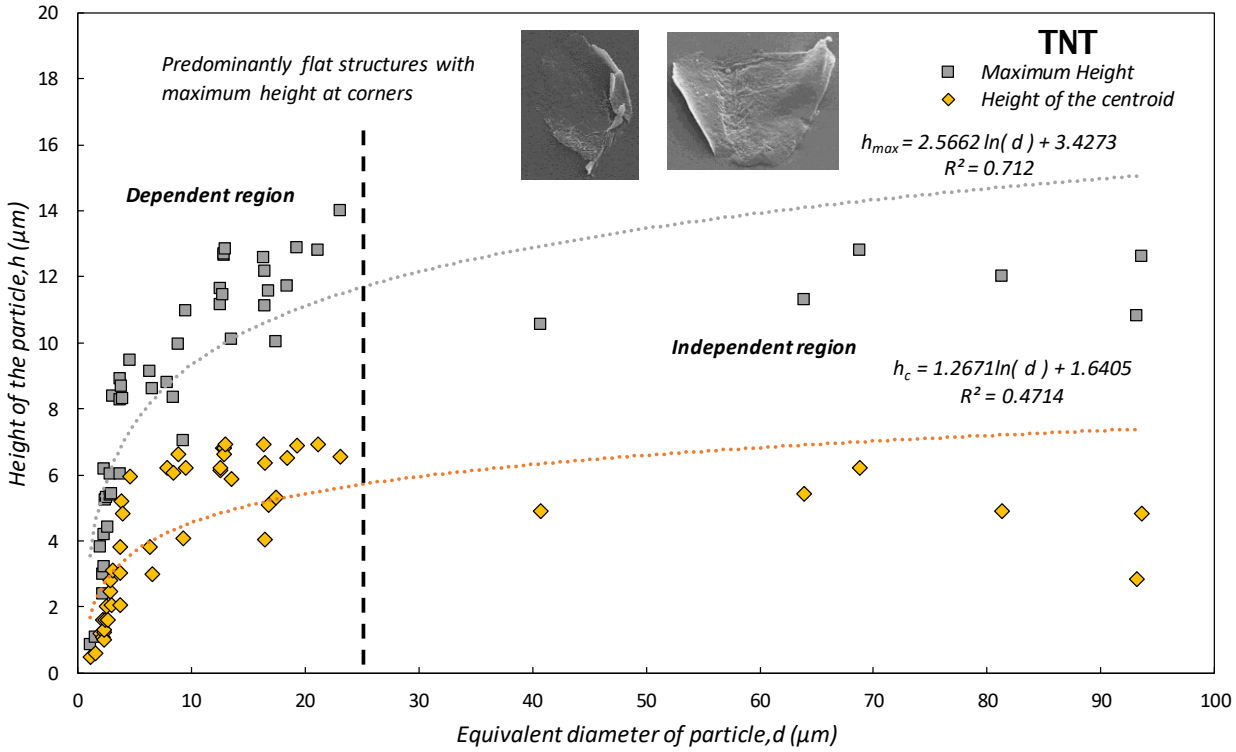


**Figure 17** *Maximum height and the height of centroid of TNT. The morphology was examined extensively, and no trend was observed in the morphology. The particles are predominantly flat structures with mass centered around the corners.*

As in the case of RDX, the majority of the particles are in the 0-25 micron equivalent diameter region. As we observe that the dry transfer method for deposition of RDX does not produce many particles with an equivalent diameter greater than 25 microns (Figure 6 and Figure 17), more precise

fit can be found for these particles. Figure 18 shows the TNT particle analysis limited to 25-micron equivalent diameter.

For particles in dependent region,

$$h_{max} = 3.7906\, ln(d) + 1.6012 \tag{7}$$

$$h_c = 2.2951\, ln(d) - 0.0998 \tag{8}$$

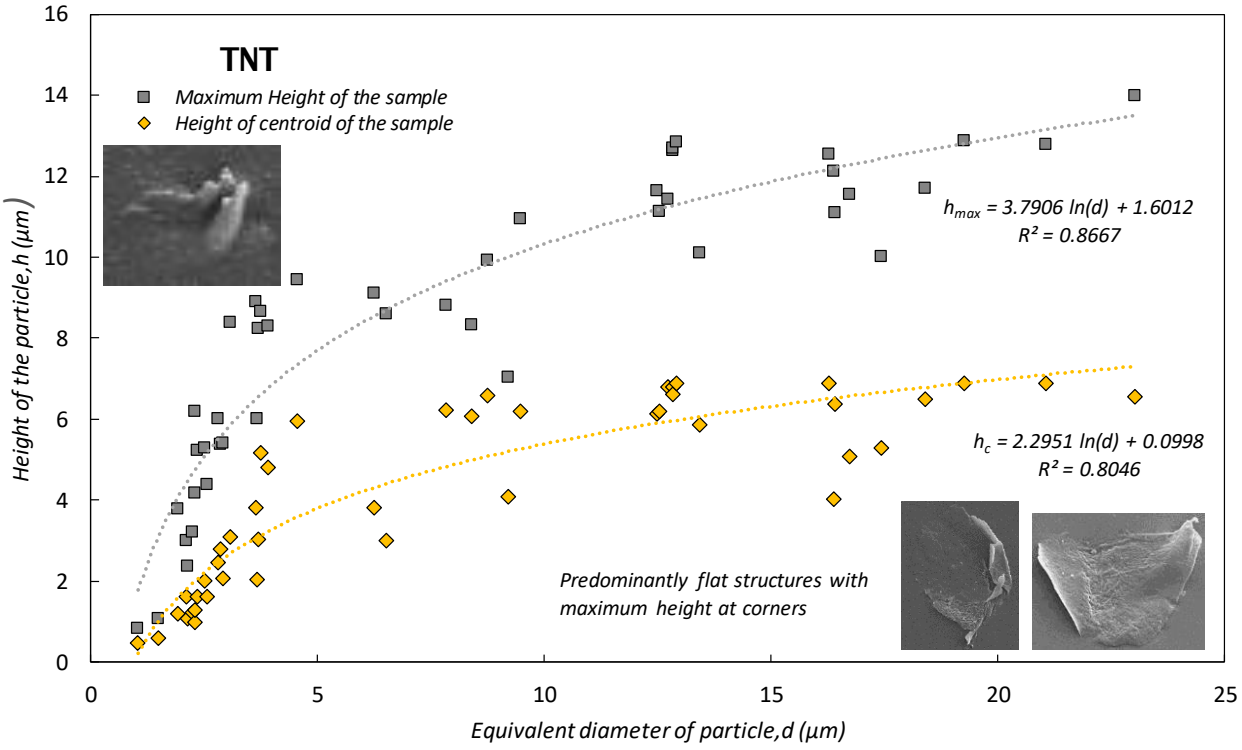


**Figure 18** *Maximum height and the height of centroid of TNT binned up to 25 μm. The maximum height of the sample and the height of centroid for TNT have a logarithmic relation with the equivalent diameter. Centroid height computed using optical profilometer measurements.*

### 2.4.3 **Limitations of the Method**

Further study will be needed to calculate the volume of the particle independently of profilometer assumptions. The gaps between the raised edges and substrate can be estimated using angled SEM. This can be done by combining data from profilometer and DEM calculations (under development). This issue is likely to affect both RDX and TNT particles.

### 2.4.4 **Aspect Ratio: Shape Factor**

Many major particle microscopic sizing techniques assume sphericity and generate shape-biased results. Few techniques use the account for 'Aspect Ratio.' Aspect ratio is the ratio of the width to the height of an image. More formally, it is the ratio of the minimum ferret diameter to a maximum ferret diameter. This parameter quantifies the "squareness" or "roundness" of an object. The aspect ratio of 1 represents a circle or a square, while a line has an aspect ratio close to 0. These approaches are appropriate for two-dimensional objects but have little relevance to aerodynamic resuspension scenario as they neglect the height of the object.

For 3- D shape (particle), we defined the Shape Factor a function of the height of centroid of a particle. The shape factor lets us comment on the morphology in comparison to the whole set. For this study, we define the nondimensional parameter, Shape factor as:

$$Shape\ Factor,\ S_f = \frac{h_c}{\sqrt{l_{min} * l_{max}}} \tag{9}$$

where,

$h_c$ is the height of the centroid,

$l_{min}$ is the minimum length on a box that fits a particle on a 2D Plane, and,

$l_{max}$ is the maximum length on a box that fits a particle on a 2D plane.

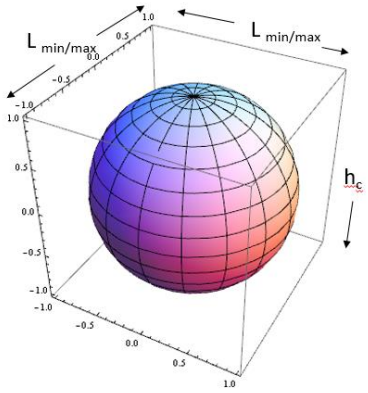


**Figure 19** *Calculation of shape factor for a spherical body.*

Shape factor using Equation (9) is computed for RDX and plotted against the equivalent diameter as shown in Figure 20.

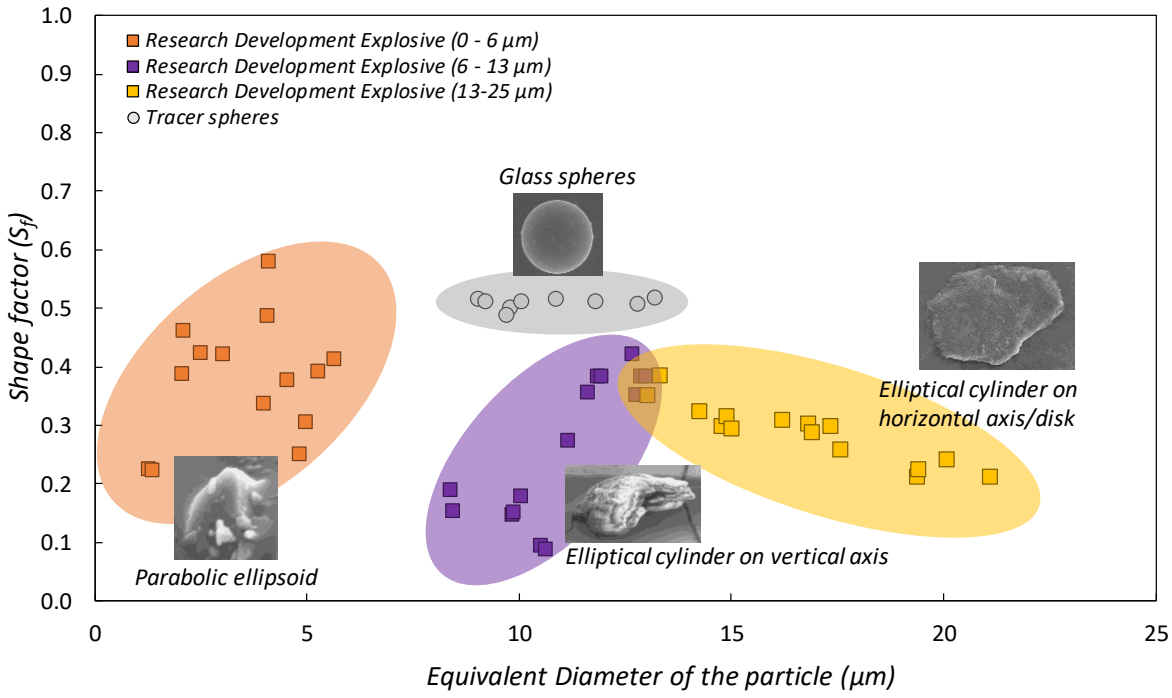


**Figure 20** *The Shape factor is plotted against the equivalent diameter. All RDX particles < 5 µm are approaching high aspect ratio similar to the spherical particles. The shape factor of particles larger than 15 microns reduces.*

The shape factor analysis of RDX shows that the particle below 5 μm is closer to the spherical structure. However, the contact area for these particles (defined by $l_{min}$ and $l_{max}$) can be high due their orientation with the surface. The better estimation of contact area can be determined if the particle curvature near the surface is quantified. The shape factor can be used as a non-dimensional parameter in aerodynamic resuspension and particle adhesion studies if related to the van der Waals forces calculations as shown later in Chapter 3.

Further work is required to characterize other particle types and to combine the SEM and optical profilometry to develop digital models and characterize the frontal and contact areas and calculate aerodynamic drag adhesion force acting on the particle.

# **Chapter 3.** Resuspension Rates with an Aerodynamic Flow Cell

## 3.1 Background

Microparticle adhesion and removal are critical in many applications, including non-contact sampling, environmental and occupational health assessments, industrial applications, and surface cleaning. In a previous study [24], we proposed an aerodynamic method to calculate the drag and lift forces acting on the particle in a flow boundary layer; the adhesion force was derived from the moment balance required to initiate the rolling motion of the particle. The geometric parameters needed to construct the moment balance were obtained from previously published models. Resuspension of silica microspheres in the range of 12-26 μm in diameter from a smooth glass surface is determined experimentally using a flow cell with known wall shear stresses. The aerodynamic method enables the calculation of adhesion force in complex particle/surface systems for different environmental conditions, surfaces, and particle properties. The method provided insight into the relationship between the wall shear stress and the aerodynamic particle resuspension and can be used to study the effects of surface roughness and a broad range of environmental conditions. A similar setup was used to investigate the resuspension of trace residues.

## 3.2 Aerodynamic Flow Cell

A 3D printed aerodynamic flow cell was used in this work, as shown in Figure 21, included a rectangular air flow cell channel formed by two parallel glass plate surfaces. The aerodynamic flow

cell was 3-D printed using high-quality PolyLactic Acid filament (PLA) to improve the fit of the components.

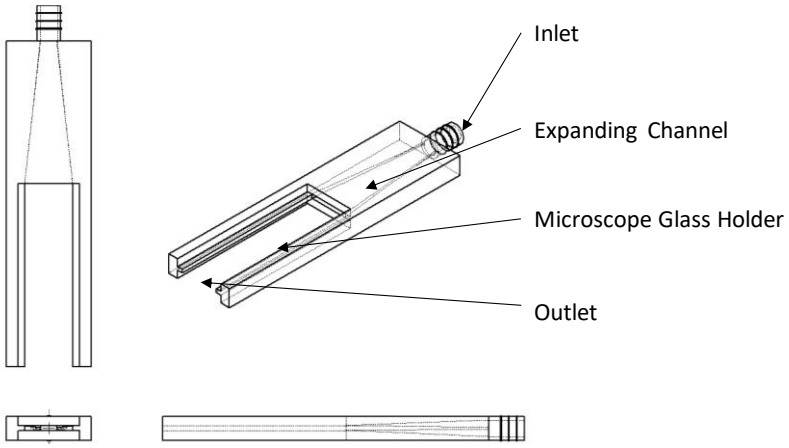


**Figure 21** *The Aerodynamic flow cell used to interrogate the removal rates of RDX, TNT, and surrogate particles. The aerodynamic flow cell was 3-D printed using high-quality PolyLactic Acid filament (PLA). It houses two glass slides: one of them has sample deposited on it and the other acts as a wall.*

The geometry consists of a cylindrical inlet, a transient contraction channel and the cuboidal section for glass slides. The inlet section has an inner diameter of 7mm and length of 15mm, and the contraction section has a length of 45mm, at last, the height of the channel is set at 1 mm. Standard 25 x 75 mm glass slides (Sigma-Aldrich, St. Louis, MO) were used for this study. The upper glass slide acted as a wall as well as provided a viewing window for microscopic visualization. The lower glass slide was coated with the particles that were interrogated with different shear flows. One end of the channel was connected to an airflow supply through an expanding channel, and the other end was left open to allow airflow to exit into ambient.

## 3.3 Experimental Setup

Experiments are conducted to determine the aerodynamic conditions required for resuspension of the particles. Figure 22 shows a schematic of the experimental setup. The flow cell housing is fabricated using 3D printing. The compressed shop air provides flow for the experiments; the air is filtered, the feed pressure and the flow rate is adjusted using pressure regulator (ARG20, SMC, Inc., IN).

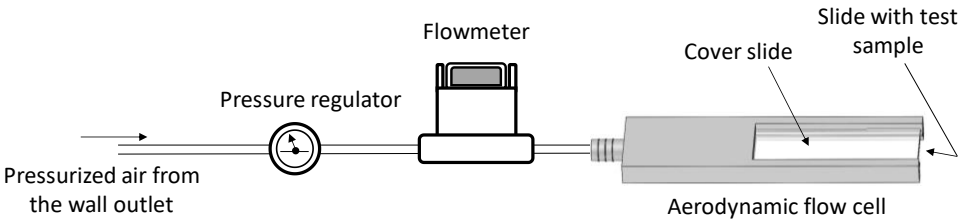


**Figure 22** *The aerodynamic flow cell setup used to study the removal rates of surrogates, RDX and TNT from a glass surface. The flow is controlled using a pressure gauge, and flow is determined by a calibrated flow meter. Removal rates are evaluated microscopically.*

The flow rate is controlled by the valve the flow rate is monitored by a digital flow meter (TopTrak 820, Sierra Instruments, Inc., CA). The metered, conditioned air stream enters the flow cell connected to the flow meter by flexible tubing. The flow rate measured during the experimental process is used as the input for the CFD simulation. The exit section had a fume absorber at about 50 m m from the outlet to contain the entrained particles from contaminating the test area. The flow cell and the nearby area was wiped with acetone regularly to avoid any residual particles.

## 3.4 Numerical Method: Calculating Aerodynamic Wall Shear Stress

Numerical simulations provide an insight into the aerodynamic forces exerted on particles in the boundary layer. Though the simulations of the flow cell do not directly provide particle force information, they establish the operational envelope and limitations of the system. The key results of

the flow cell analysis are: (i) calculated wall shear stress ($\tau_w$) values as a function of the flow rate in the cell, (ii) velocity profile in the boundary layer, and (iii) determination of the flow regime (i.e., laminar, transitional, turbulent) as a function of distance from the wall, defining the range of particle sizes that can be used in the experimental study. Figure 23 shows the 3D model of the flow cell. The computational domain includes a cylindrical inlet, transition section, and 1 mm high test section enclosed by microscope glass slides. The inlet section has an inner diameter of 7 mm and a length of 15 mm. The transition section converts the flow to the rectangular test section with minimal changes in the cross-sectional area to avoid the onset of flow instabilities; it has a length of 45 mm. The test section is confined by two microscope glass slides; it is 75 mm long and 25 mm wide. Mesh optimization is performed to resolve the viscous sublayer to capture $\tau_w$ as defined by a nondimensional wall distance of $y^+ = 5$. To resolve the flow in the viscous sublayer, we use at least three cells within this region; the first grid point is located at a distance of $y^+ \approx 1$. Further refinement of the mesh did not result in changes in the boundary layer profile. The computational domain mesh consists of about 1,000,000 quadrilateral elements.

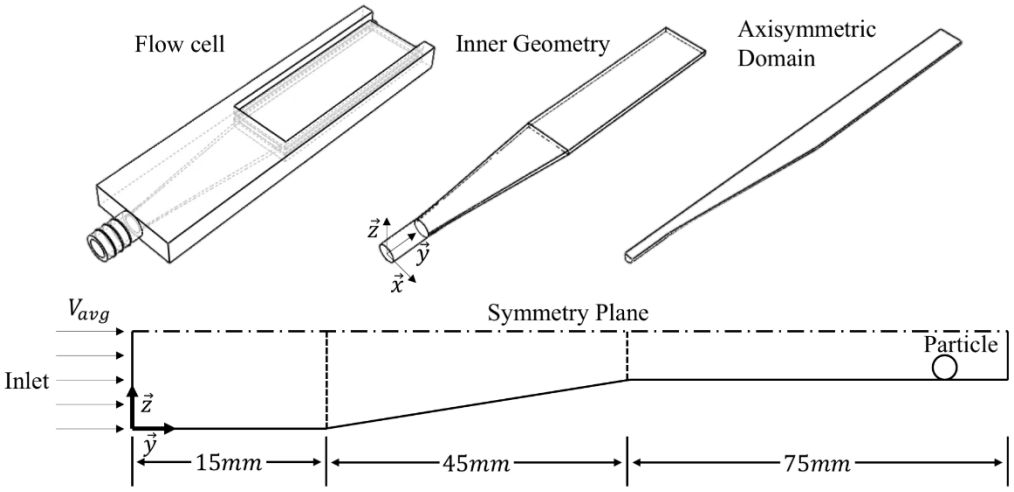


**Figure 23**. *Top: flow cell geometry; Bottom: schematic of the computational domain (not to scale). A quarter of the domain is modeled due to symmetry. The inlet is set as the velocity boundary conditions; the outlet is set the atmospheric pressure boundary condition.*

The choice of the turbulence model considers the need to resolve the near-wall boundary layer. The standard $k-\varepsilon$ model yields reasonable results for free shear flows with relatively small pressure gradients but struggles in wall-bounded flows with larger pressure gradients [25]. The $k-\omega$ model has been shown to be superior to the $k-\varepsilon$ model in the flow near the wall and transitional (laminar to turbulent) region, but it suffers from numerical instability. The Shear Stress Transport (SST) $k-\omega$ turbulence model [26] is a two-equation turbulent viscosity model which combines the best of both the $k-\varepsilon$ and $k-\omega$ models. The use of the $k-\omega$ formulation in the inner parts of the boundary layer makes the model directly applicable in resolving the viscous sub-layer. The SST formulation switches to a $k-\varepsilon$ behavior in the free-stream and, thereby, avoids the common k-ω problem of hypersensitivity to the initialization and inlet conditions. The SST $k-\omega$ model can be used as a Low Reynolds number turbulence model without secondary damping functions and is a well-suited option for this work. The inlet boundary condition for the flow is a uniform velocity profile; the velocity magnitude is determined from the measured flow rate for each experimental condition. Wall boundary

conditions are no-slip walls; the outlet is modeled as an ambient pressure boundary condition. The inlet turbulence length scale is set based on fully developed turbulent flow in a pipe to 3.8% of the hydraulic diameter.

The preliminary experimental results have shown that if the particle is exposed to the flow outside of the viscous boundary layer, where non-dimensional distance is greater than five ($y^+ > 5$), the particle removal data is not reproducible (likely due to the inconsistent nature of transitional layer flow). We determined that for the flow rate considered in this study, the linear boundary layer profile assumption is valid for particles smaller than 25 microns. Though it is possible to test for the removal of particles larger than 25 micron (due to the lower velocity associated with their removal), the linear velocity assumption is not valid; the data is not consistent.

## 3.5 Aerodynamic Particle Resuspension in a Flow Cell

The relative humidity in the experiment is measured by the RH meter, typically below 5 %. The microscope glass slides with the particle are examined, and the leading edge of the particle deposition is evaluated using optical microscopy. At the beginning of each experiment creeping flow (at ~10% of the experimental flow rate) is used to dehumidify the system for 3-4 minutes. This step is crucial as the dry air will remove moisture in the setup without removing particles. To perform time independent experiment, each test is conducted until no more particles are being removed. In a preliminary study, we found that a flow exposure time of 30 seconds is appropriate for reaching steady state at all flow conditions. Before each experiment, all parts of the flow cell are cleaned with pressurized air to ensure that no extraneous particles are introduced to the experiments. Particle deposited on the glass slide are counted before and after the removal experiments as previously

described (Section 2.3).Both the images are analyzed using MATLAB code, and image processing modules and the removal rates are calculated.

Each experiment consists of particle removal by airflow at the assigned flow rate; the removal fraction in each particle size bin (1 micron) is recorded as a single data point as shown below in Figure 24. In a typical experiment, on average 1200 particles are observed with a minimum of 40 particles in each size bin. A total of 120 experiments are performed with approximately 4200 particles in each bin size analyzed for removal. The analysis of the 50% threshold removal condition is based on $N_{total}$= 5897 particles; the minimum number of particle in each size bin is $N_{min}$=113. Since the contact area is dependent on the equivalent diameter of the particle, the removal rates as a function of equivalent diameter are used for analysis.

The surrogate particles were harder to remove at lower sizes as they are greatly affected by the morphological features of the surface like roughness and environmental factors such as RH [27]. Figure 24 shows as the size increases for the soda lime glass microspheres, the removal is proportional to the $d^{0.3615}$.

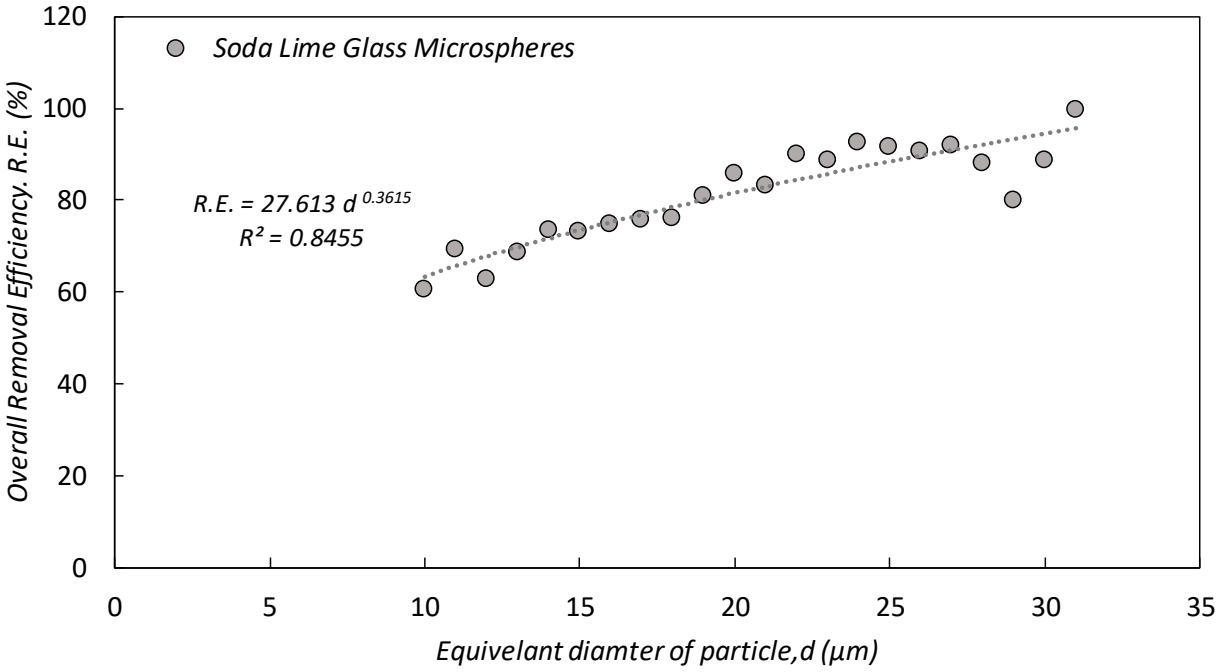


**Figure 24** *Removal Efficiency of Soda lime glass microspheres as a function of their equivalent diameter at inlet flow rate of 60 lpm. Removal of surrogate particles is directly proportional to the equivalent diameter.*

Figure 25 plots the removal rates of the trace residues of two explosives that we tested at 130 lpm in the flow cell. The shear stress value associated with this condition is *59.28 Pa*. As the size of particle increase, so does the contact area, the trace residues of explosives are harder to remove due to the strong adhesion forces between the particle and substrates. TNT was found to easier to remove than RDX when compared to the same equivalent diameter. The previous study[15] has shown that TNT has lower adhesion force in comparison to RDX, which is consistent with our study. Here the particle size is determined as equivalent particle diameter as imaged at a normal angle.

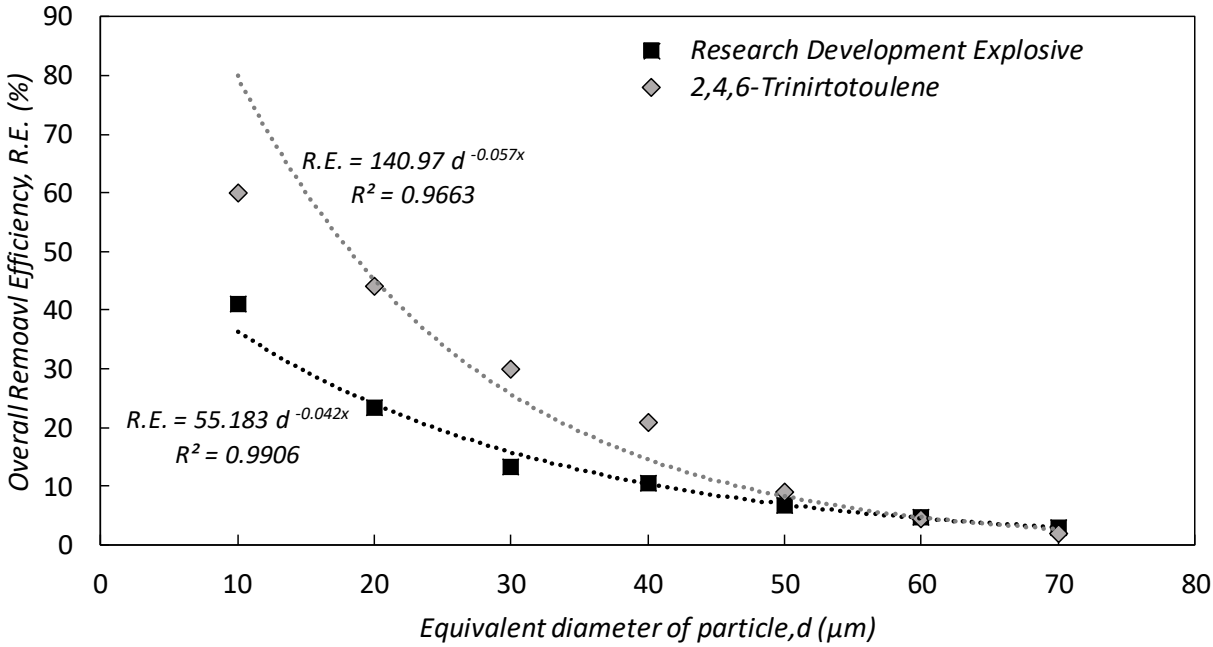


**Figure 25** *Removal Efficiency of Energetic particles (RDX and TNT) as a function of equivalent diameter. The removal of energetic particles is inversely proportional to the equivalent diameter.*

Traditionally, $\tau_w$ is considered in aerodynamic particle removal; for particles located in the linear sublayer of the flow, the shear stress value fully describes the flow at the particle location. While mathematically it is not necessary to use $\tau_w$ for the calculation of the aerodynamic and adhesion forces, it is useful for characterizing the flow independently of the particle size and morphology for comparisons with aerodynamic particle removal in less controlled removal scenarios.

For the energetic material, there is an inverse relationship between the equivalent diameter of the particle, the shear stress required to remove 50% of larger TNT or RDX particle has to be greater than for the smaller particle. This can be explained by the decreasing relative height (shape factor) of TNT and RDX deposit for particles with larger equivalent diameters. As the size of x-y increases, hence the contact area, the height stays relatively constant; it gets harder to remove the particle.

**Table 3** *Relation between the removal rates and the equivalent diameter of all the particle entrained in the aerodynamic flow cell.*

| Material | Relation between R.E and *d* |
|---|---|
| Soda Lime Glass Microspheres | R.E. = 27.613 $d^{0.3615}$ |
| Research Department Explosive | R.E. = 55.183$e^{-0.042x}$ |
| 2,4,6-Trinirotoulene | R.E = 140.97$e^{-0.057x}$ |

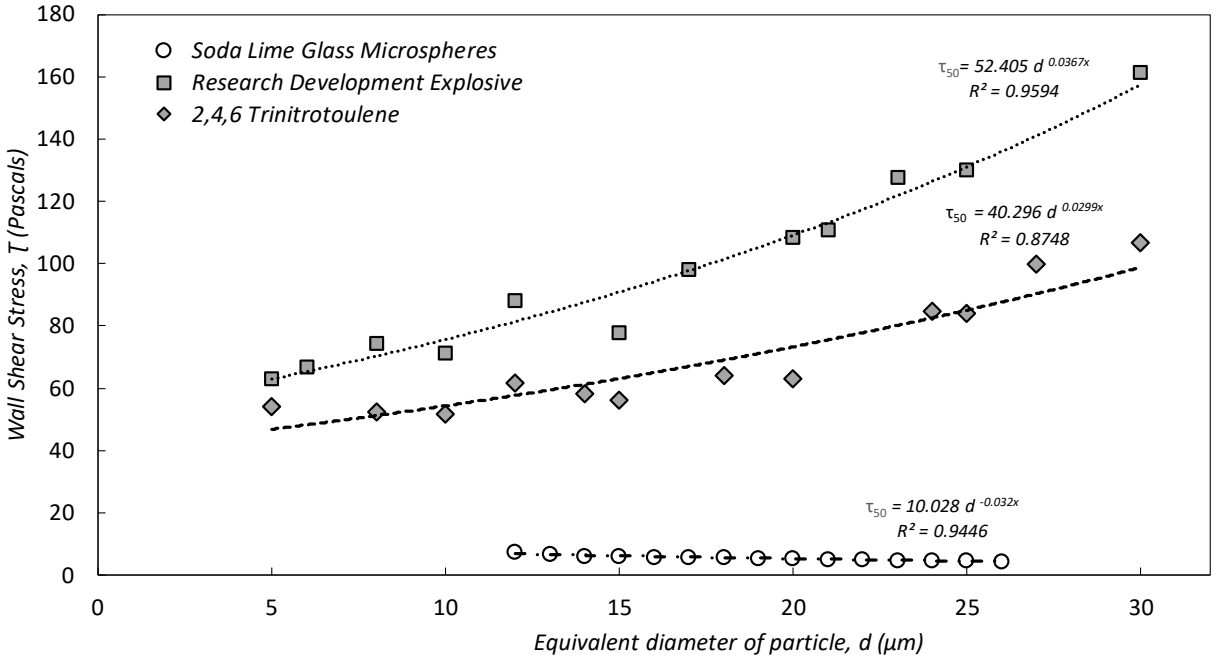


**Figure 26** *The critical wall shear stress required for 50 % removal ($\tau_{50}$) as a function of the size of the particle. For explosive particles, the force needed to remove the particle exponentially increases as the particle size increases which is inverse for the trend observed for surrogate particles.*

The critical wall shear stress required for 50 percent removal of energetic particles was computed with the data obtained from the numerical simulations and the removal data obtained from the experiments. The critical wall shear stress ($\tau_{50}$) is exponentially dependent on the size of the particle. The empirical relations have been tabulated in Table 4.

**Table 4** *Relation between the critical wall shears stresses for 50 percent removal and the equivalent diameter of all the particle entrained in the aerodynamic flow cell.*

| Material | Relation between R.E and $d$ |
|---|---|
| Soda Lime Glass Microspheres | $\tau_{50} = 10.028e^{-0.032d}$ |
| Research Department Explosive | $\tau_{50} = 52.4056e^{0.0367d}$ |
| 2,4,6-Trinitrotoluene | $\tau_{50} = 40.697e^{0.0284d}$ |

The threshold shear stress associated with 50% particle detachment ($\tau_{50}$) are determined experimentally for each particle size and are compared with numerical results. Although in this work the critical stress corresponds to the resuspension of 50% of the particles as it provided the most consistent results, other thresholds can be used. Shear stress calculations guide the experimental design, provide boundary layer characterization independent of particle size and morphology and can be used for the design of the particle removal apparatus.

We hypothesized that *the frontal area, thus the height 'h' of the particle has a direct correlation with the resuspension rates.* Figure 27 plots the critical wall shear stress versus the height of a sample of RDX. We observe the following trends:

- For h < 6 μm, the critical wall shear stress does not vary by a lot as a function of height as the aspect ratio of the particle does not change by a lot.
- For 6 μm < h < 8 μm, the critical wall shear stress does vary by a lot as the morphology of the particle change rapidly, and there is a big slump in the aspect ratio as discussed in Figure 20.
- For h < 8 μm, the critical wall shear stress varies as a function of the height as the aspect ratio is highly influenced by the smaller heights and larger equivalent diameters.

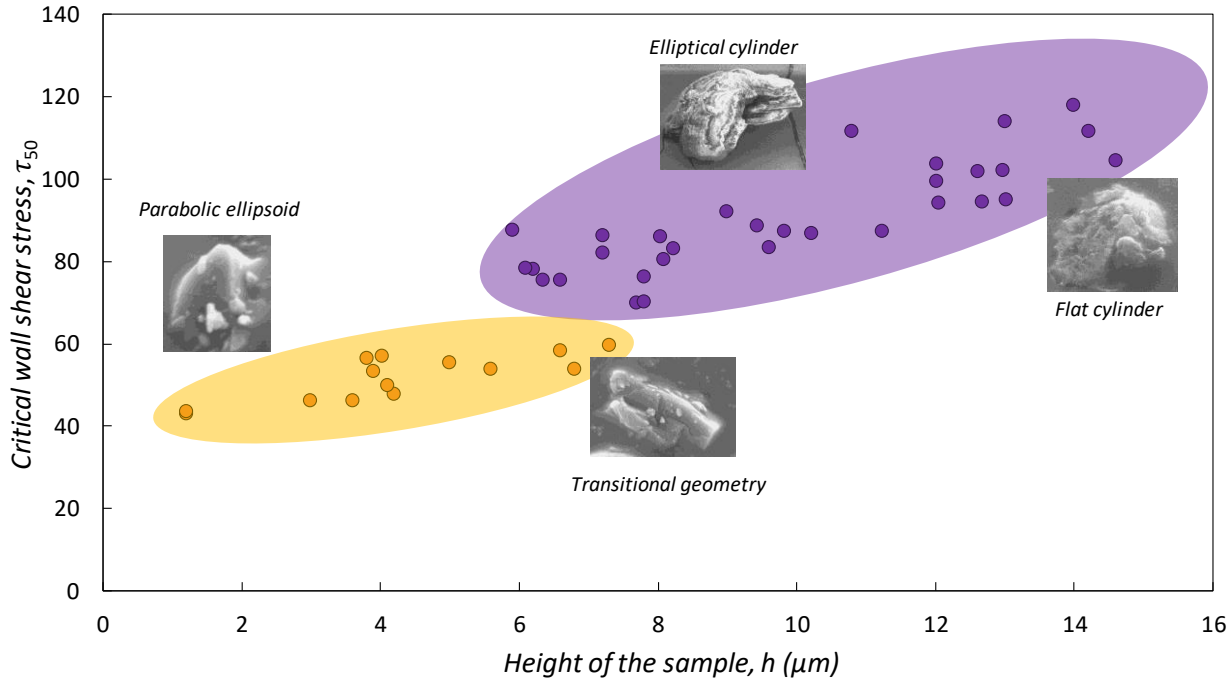


**Figure 27** *The critical wall shear stress required for 50 % removal ($\tau_{50}$) of RDX dry deposited on the glass slide as a function of the height of the particle. Two distinct regions were observed with different trends.*

Similarly, for 2,4,6 Trinitrotoluene (TNT) the critical wall shear stress required for 50 percent removal of TNT particles plotted against the height of the same as shown in Figure 28. Alike RDX, two distinct regions with different trends are observed.

- For h <7 μm, the critical wall shear stress does not vary by a lot as a function of height as the aspect ratio of the particle does not change by a lot.
- For 7 μm < h < 10 μm, there is a change in morphology of the particle, and they are require
- For h > 10 μm, the critical wall shear stress increases rapidly as the equivalent diameter increase rapidly as compared to the height of the sample.

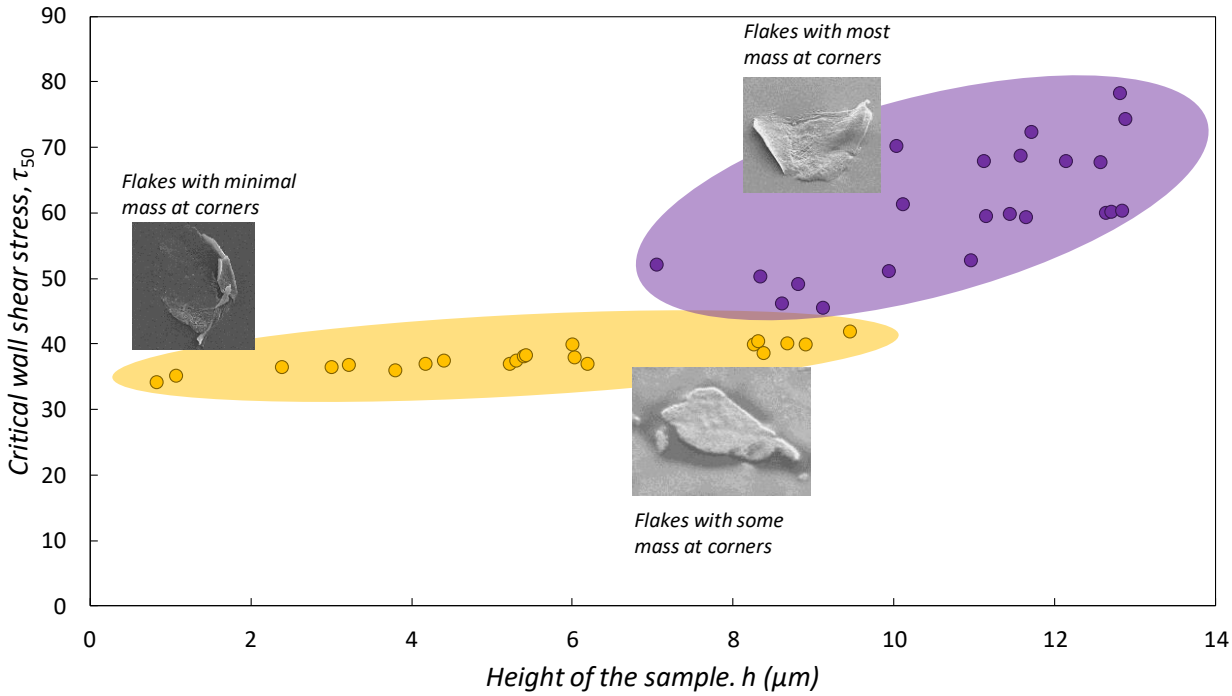


**Figure 28** *The critical wall shear stress required for 50 % removal ($\tau_{50}$ ) of TNT dry deposited on the glass slide as a function of the height of the particle. Two distinct regions were observed with different trends*

The threshold wall shear stress for all the three types of particle are plotted as a function of height for comparison as shown in Figure 29. Zone 1 for RDX and TNT (marked as mustard yellow in *Figure 27* and *Figure 28*) shows no dependence on the height of the particle. This is a similar trend observed in the case of soda lime microspheres. Morphological changes in zone 2 cause rapid change in the critical wall shear stress required to entertain those particles.

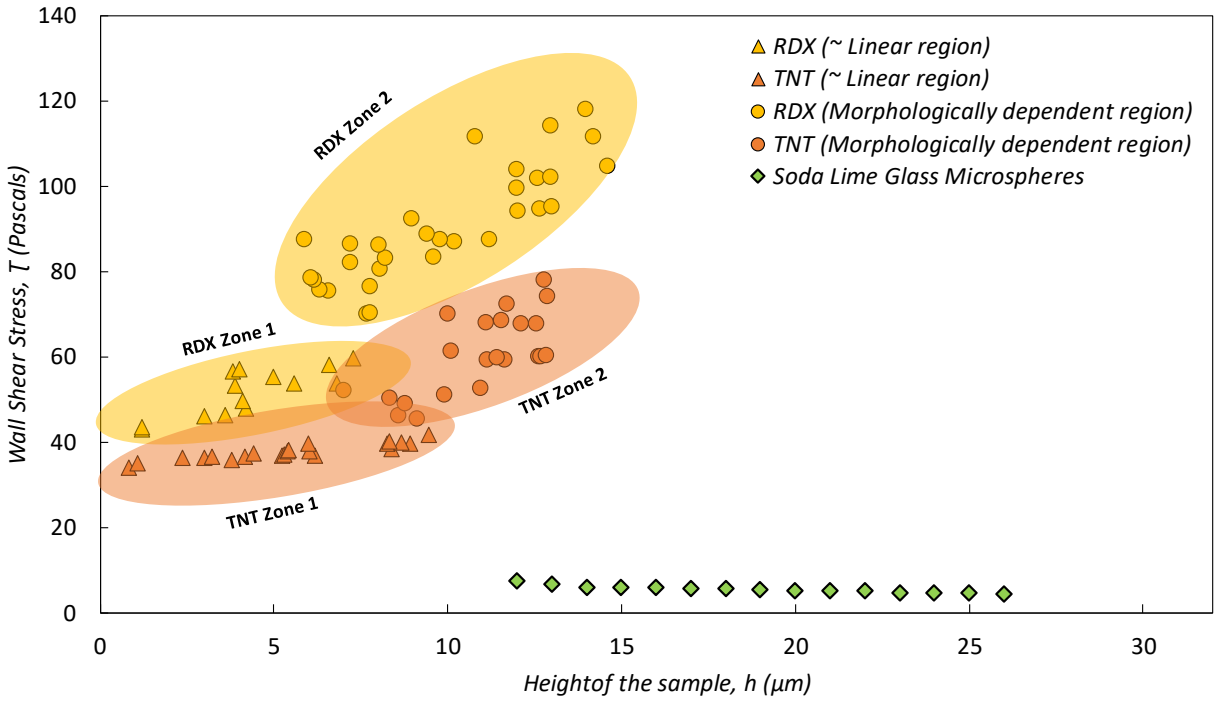


**Figure 29** *Critical wall shear stress ($\tau_{50}$) as a function of the maximum height of the sample (RDX, TNT and soda lime glass microspheres). The soda lime glass microspheres show no dependence of height on the removal rates. Similar trend was observed for the case of RDX and TNT when $h_{max}$ < 6μm.*

No or very little dependence of height has been observed on the removal rates of smaller particles of trace residues of RDX and TNT. One of the reasons is that the contact area between the particle and the surface increases linearly with the frontal particle area. Particle aerodynamic drag is proportional to the frontal particle area while the particle adhesion force is proportional to the particle/surface contact area. In the linear h=f(d) region both force terms balance each other. In the constant height region, the frontal area grows as linear with the increase of the diameter, but the contact area and thus the adhesion force increases as $d_p^2$, resulting in the increase of the threshold shear stress values as a function of particle height.

# **Chapter 4.** Trace Explosive Collection and Detection

## 4.1 Background

As any analytical instrument, trace-based explosives detection (ETD) systems have limitations in sensitivity, selectivity, and dynamic range; size and cost are often an issue. Miniaturization of systems to the bench top or even handheld levels has great potential. The electronic-based sensors based on microelectromechanical systems (MEMS), and nanotechnology based systems (or Nano-electromechanical systems, NEMS), show promise for improvements in sensitivity, selectivity, improved alarm rates, size, and cost. While extensive research is conducted on improving or redesigning these systems, efficient and effective collection media for this new generation for samplers is needed. The cost of consumables for such systems is high, increasing the overall operational costs. In this work, we characterize a metal fiber mesh for the use of collection media which is the perfect alternative to current media due to following reasons:

(a) Reusable as they can be thermally cleaned,

(b) Compatible with existing and evolving detection systems, and,

(c) Low-cost ($ 2/ $m^2$)

## 4.2 Impinging Jet Setup

To characterize the particle capture efficiencies on metal fiber mesh, the particles can be aerosolized; then the laden particle flow can be driven through the collection media. The filtration (or capture) efficiency can be determined gravimetrically based mass gain on the metal filters and breakthrough mass. An impinging jet setup is used for particle aerosolization and sampling flow generated through

the mesh to capture the entrained particles. Soda Lime glass (Cospheric LLC, Santa Barbara, CA) of sizes ranging from 8 μm – 100 μm used previously in entrainment studies was used for this study. Figure 30 shows the setup used in the experiments. The sampling fixture houses the opposing jets and filter holder assembly; the fixture is placed onto a test coupon to prevent excessive particle loss. The sample aerosolization is provided by slit jets that resuspend the test particles placed on the test coupon. All the components have been 3-D printed using high-quality PolyLactic Acid filament (PLA) to improve the fit of the components. The particle laden flow is aspirated into the sampling port of the fixture by the vacuum connection generated by a linear piston pump (5250 Thomas Inc., Sheboygan, WI) is controlled by a 120 VAC variable transformer (ISE, Inc., Cleveland, OH). The sampling flow is varied between 0-100 liters per minute is quantified with the help of TSI 4100 flow meter.

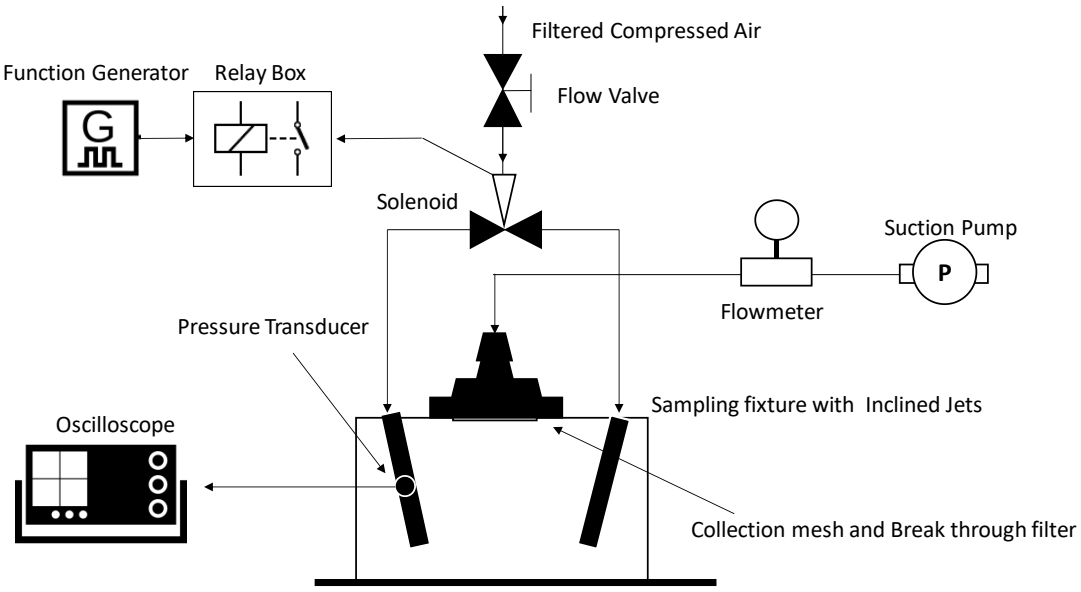


**Figure 30** *Experimental setup for evaluating capture efficiency of resuspended particles from the surface. The particles are resuspended from the surface by the pulsed slit air jets and aspirated into the sampling port. The removal and capture flow rates are controlled.*

## 4.3 Sample Aerosolization

To perform capture experiments, particles are first aerosolized inside the sampling fixture enclosure. A brushed aluminum 6061(McMaster-Carr) is used a test coupon for particle deposition. The surface is cleaned with pure ethanol and dried using pressurized air. The surface roughness of the deposition area is measured using Mahr XR 20 surface profilometer. The surface roughness of the deposition area is 4.58 μm ± 0.26 μm. Monodisperse silica microspheres (Cospheric LLC, Santa Barbara, CA) of sizes ranging from 8 μm – 100 μm are deposited on the surface by suspending them over the deposition area. Any particles outside the 50 x 50mm sampling area are removed by wiping with lint-free wipes (Kimberly Clark Inc., Irving, USA) Figure 31 shows the 3D view of the sampling fixture, the opposing slit jets are used for particle aerosolization.

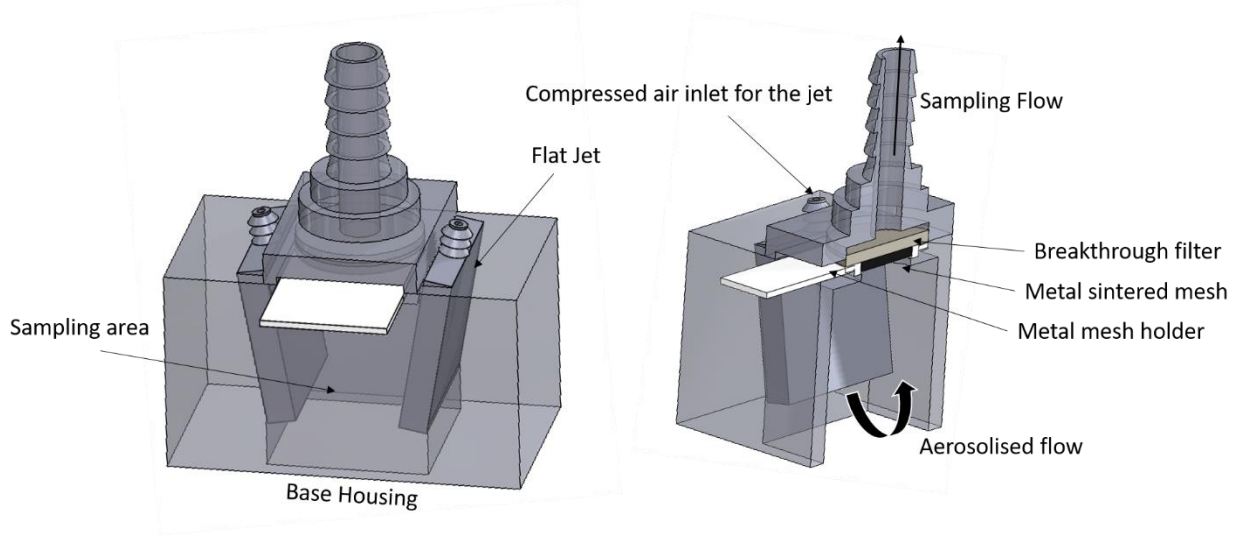


**Figure 31:** *Impinging flat jet setup for the collection of fine particles. The sampling fixture houses two jets inclined at 10 degrees with the normal. The aerosolized flow percolates through filter assembly which consists of the metal sintered mesh supported by a Teflon coupon and a breakthrough filter.*

The jets are 35.4 mm long and 1 mm wide and are inclined at 10 degrees from normal to facilitate the effective particle resuspension and aerodynamic trapping [28-30]. Sufficient shear stress on the surface

is produced to facilitate particle resuspension [24]. The pressure for the jet is supplied by the filtered compressed shop air. To control the duration of the air jet pulse in-line solenoid (B- Cyro series, Gems Sensors Inc., Plainville, CT) is controlled by a BK Precision 4053 function generator. To ensure the pulse repeatability, jet gauge pressure is monitored by an SSI P51 pressure transducer. The nozzle width and jet pressure are kept constant at 35.4 mm and 20 psi respectively.

## 4.4 Particle Capture

The capture mechanism is dependent on the aerodynamic size of the particle and pore size of filter media. Particle size is of particular importance because particle liberation from surfaces by air jets and aerodynamic transport are highly dependent on particle diameter. For particle collection, several capture mechanisms are typically considered: impaction, interception, diffusion, electrostatic deposition, and straining. For the larger particles straining is often the predominant mechanism it occurs when the smallest particle dimension is greater than the distance between adjoining filter fibers and the particle gets trapped in the filter media. This mechanism is likely to be dominant for particles with large Stokes numbers and high bounce characteristics.

Sintered metal fiber matrix (Bekipore substrate, Bekaert corporation, Atlanta, GA) of different porosities have been used to collect the fine particles. The 25x25mm piece of the sintered metal fiber matrix is mounted in the Teflon holder. A breakthrough filter (1-micron class fiber filter) is placed after the collection substrate as shown in Figure 31. To perform the gravimetric analysis, the components are weighed before and after by Mettler AE260 analytical balance. The balance calibration was regularly checked for any residual values before measuring any new component. The capture efficiency was quantified by the ratio of change in mass of the collection substrate to the sum of the change in mass of collection substrate and mass of breakthrough filter.

$$\text{Capture Efficiency, C.E. (\%)} = \frac{\Delta m_{CS}}{\Delta m_{CS} + \Delta m_{BF}} \quad (10)$$

where,

$\Delta m_{CS}$ = Change in mass of the collection substrate, and,

$\Delta m_{BF}$= Change in mass of the breakthrough filter.

## 4.5 Capture Substrate Characterization

### 4.5.1 Pressure Drop Across the Substrate

Four different sizes of sintered metal mesh are used to collect the resuspended PM. The equivalent diameter of the pores is calculated by the bubble point test [ASTM 2011] and was found to be consistent with the specifications. Due to the variability in the collector dimensions and the flow rates in the design of sampling devices, a normalized parameter for assessment of substrate's collection properties is required. In air filtration applications, researchers and filter manufacturers use face velocity as an independent parameter to account filter flow rate and the filtration area. Typically, a significant increase in the face velocity (over the rated) has a dramatic negative impact on filter efficiency. Here we calculate the face velocity based on the measured flow rate and the area of the collection substrate as a ratio of the flow rate to the open area of the filter. The area of the collection area is fixed (A=1180 $mm^2$) and the flow rate is varied in the range of 1-94 slpm.

The pressure drop across the collection substrates is measured as a function of face velocities by varying the flow rate of the vacuum pump. Using Darcy's Law, the pressure drop across the substrate can be written as the filtration velocity/face velocity times the filter resistance constant (which depends on the physical characteristics of the filter medium such as the filter pore size, filter material, and filter thickness). Figure 32 plots the pressure drop across the substrate as a function of sampling

flow velocity. The pressure drop increases linearly with the face velocity, revealing that the aerosol flow across the test filter is laminar [31].

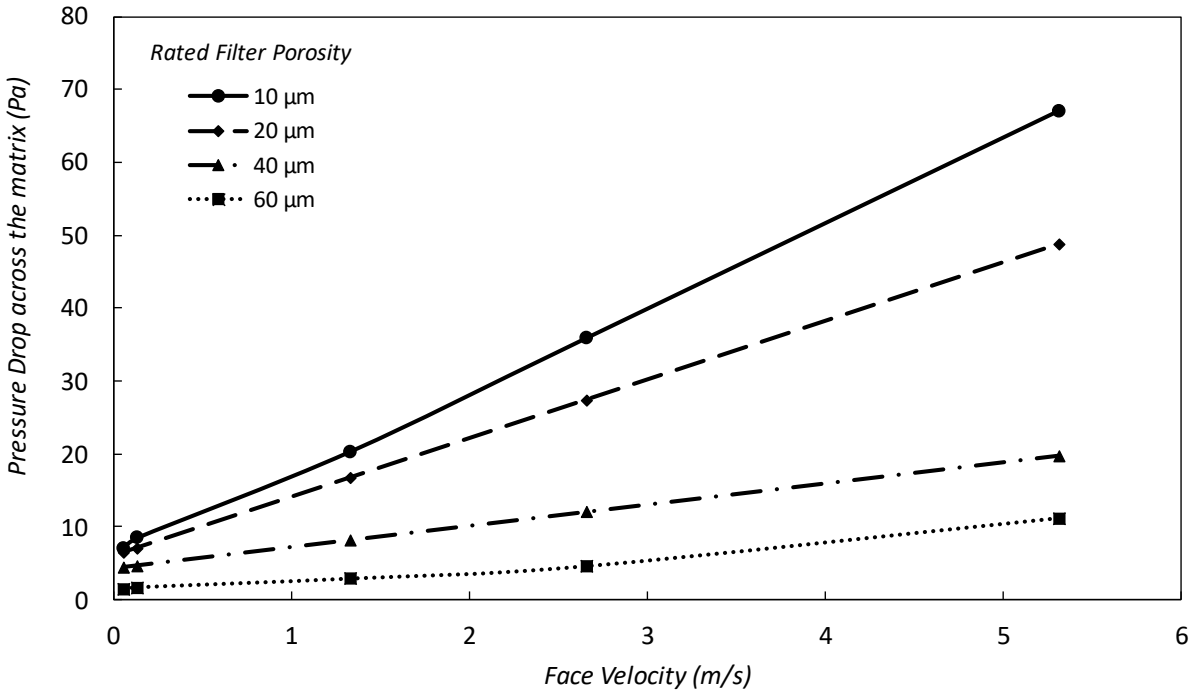


**Figure 32** *The pressure drop across different meshes at different face velocities. The slopes are linear for all mesh porosities; the pressure drop for highest porosity is lowest.*

As expected the BL60 (60-micron porosity) has the lowest and BL10 has the highest pressure drop in the operating sampling velocity range of 0 to 100 liters per minute. The particle loading on the filter is dependent on the number of particles and size of the particles; the significant loading will change the flow resistance as the particles are captured in the voids in the filter media. This effect is well characterized elsewhere [32] [33] and it is not considered in this study.

### 4.5.2 Particle Capture

Two independent parameters for characterization of sampling media are considered, these face velocity and the particle size. The particle size is chosen based on the representative particle sized for

the particle size distribution in the fingerprint. The face velocity effect is important in concerning the sampling flow rate and the sampling device construction.

To determine the effect of the particle size we performed the experiments at a constant face velocity of 5 m/s (sampling rate of 94 lpm). All four collection media substrates are evaluated for particle size range 8-100 micron. Twelve experiments are performed for each particle size/substrate porosity combination. Figure 33 shows the collection efficiency is the highest for substrates with smaller pore sizes. The 50% collection efficiency roughly corresponds to the rating of the substrate.

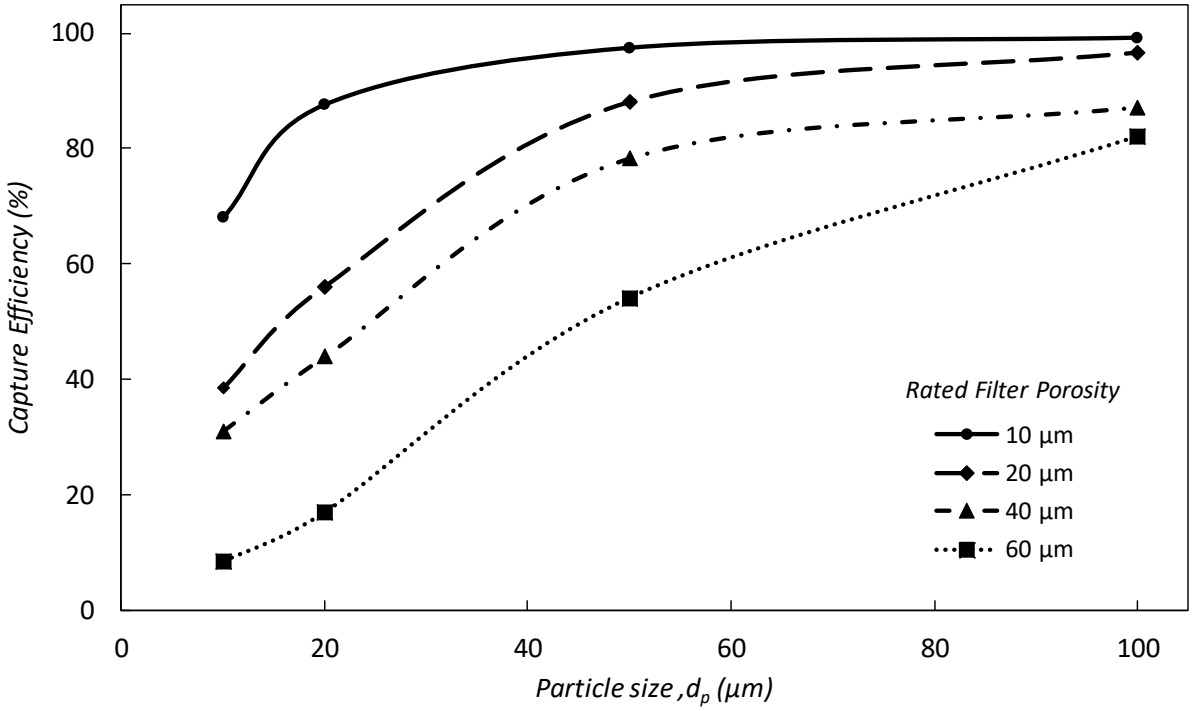


**Figure 33** *The capture efficiency of metal sintered meshes for different particle diameters (10 μm, 20μm, 50μm, 60μm).*

The effect of the face velocity on the capture efficiency was evaluated for 20-micron silica microspheres. Face velocities are varied between 0.1 m/s – 5 m/s by changing the sampling flow rate. Figure 34 shows that the collection efficiency does not change significantly with face velocities.

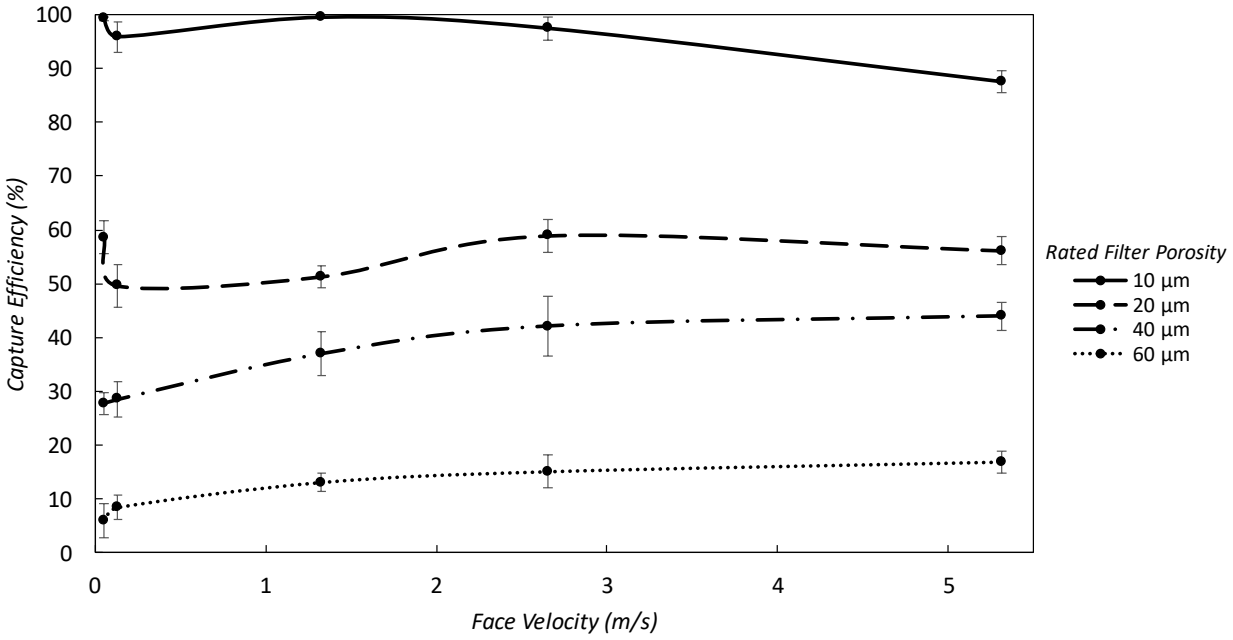


**Figure 34** The capture efficiency of metal sintered meshes with different face velocities for 20µm Silica microspheres

Fifteen experiments for each data point are performed. Similarly, to Figure 33, the plot shows that the collection efficiency increases as the porosity of the collection mesh decreases.

The sintered metal substrates provide a low-cost, efficient surface suitable for collection of aerosolized trace particles and compatible with wide range of analysis methods such as IMS. Further work on thermal reusability of the fiber mesh and its adaptability to vapor collection will be a natural extension of this work.

# **Chapter 5.** Results and Discussion

## 5.1 Summary of Findings

### 5.1.1 Morphology Analysis of Trace Explosive Residues

In the morphology analysis work, we tested the hypothesis that *the frontal area, thus the height 'h' of the particle has a direct correlation with the resuspension rates*. We use the combination of scanning electron microscopy (SEM) and optical profilometer to quantify the height of trace residues of *Trimethylenetrinitramine* (RDX) and *2,4,6- Trinitrotoluene* (TNT). Digital Elevation algorithms developed in MATLAB with SEM images of a particle at every 15 degrees from each corner were used to quantify the height. The method is in calibrated with the quantification of the height of precision microspheres. The primary findings were as follows:

- The method is in good agreement with quantification of height for glass microspheres.
- For RDX particles, three morphologically similar sets are found as a function of particle size.
- The TNT crystals are found to be thinner, and their maximum height was recorded at the raised edges
- For TNT particles, there is a logarithmic relation between the maximum height and diameter of the particle for TNT while the maximum height for RDX was proportional to $d^{0.7235}$.
- As the size of the particle in x-y increases, hence the contact area, the height stays relatively constant; it gets harder to remove the particle.

- A nondimensional parameter, shape factor has been defined for predicting removal rates as a function of morphology. The shape factor analysis of RDX shows that the particle below 5 μm is closer to the spherical structure.

### 5.1.2 Aerodynamic Particle Resuspension

In particle-surface adhesion work, we tested the hypothesis that *the combination of numerically calculated aerodynamic forces acting on the particle and the particle detachment experiments in a controlled wall shear stress environment will lead to the estimation of threshold forces required for detachment of trace residues of energetic particles*. The aerodynamic method for determining the particle adhesion forces relies on the estimation of forces acting on the particle in the boundary layer from the CFD or the available analytical or empirical relationships. A detachment of silica microspheres from a smooth glass surface is studied experimentally in a flow cell to determine the threshold force values independent of non-uniform morphology required for particle detachment. A similar model is then applied to trace residues of two primary energetic particles: *Trimethylenetrinitramine* (RDX) and *2,4,6 Trinitrotoluene* (TNT). The primary findings are related to the method development and results obtained from this approach, which, in summary, are:

a) RDX dry deposited on a glass slide can be classified into 3 sets of morphologically similar particles as a function of the equivalent diameter. Morphology of TNT did not have any trends. Most of the particle of the TNT were very flat with mass centered around corners which attributed to their maximum height during the analysis

b) Based on the best fit, the maximum height of the sample is proportional to $\sim d^{0.7235}$ for RDX and height increases logarithmically for TNT.

c) The threshold Shear stress associated with 50% particle detachment ($\tau_{50}$) has exponential relation with the equivalent diameter of the particle (Table 4)

### 5.1.3 Particle Collection on Porous Substrates

A porous metal fiber mesh has been characterized for use as a collection media. The sintered metal substrates provide a low-cost, efficient surface suitable for collection of aerosolized trace particles and compatible with wide range of analysis methods such as IMS. The effects of particle size ($d_p$) and face velocity were considered to find their influence on the capture efficiency on a porous metal filter media. Following are the outcomes of the study:

- *The pressure drop increases linearly with the face velocity.*

  The pressure drop across the substrate is a function of the porosity of the metal mesh. The operating conditions and the pressure drop across a filter may determine the type of mesh to be used for the sampler design. While the capture efficiency is higher for the substrates with the lower porosity, the flow rate desired for non-contact sampler operation may not be achievable at the high flow resistance values.

- *Collection efficiency is independent of the face velocity.*

  The higher of face velocity does not affect the capture efficiency on the sintered fiber metal matrix for all porosity values.

- *Collection efficiency is proportional to the size of the particle and inversely proportional to the porosity of the collection media.*

As observed in Figure 34, the collection efficiency increased with an increase in particle size and decreased the porosity of the collection media. Operating conditions and the target size of the trace particles [7] will determine the choice of collection media to be used for the sampler.

## 5.2 Synopsis of Innovations and Inventions

The method for calculating the particle detachment threshold independent of particle type in a controlled environment has been developed. The aerodynamic method allows for the collection of large amounts of data irrespective of removal mechanisms, allowing for an insight into the actual statistical behavior of particles undergoing resuspension. The method also provides insight into the relationship between the $\tau_w$ and particle rolling and sliding detachment. The wall shear stress provides boundary layer parameterization and can be utilized for the particle detachment studies independent of particle properties and environmental conditions (which is essential in case of trace residues). The relationship between the wall shear stress and particle removal efficiency can assist in the experimental design, particle resuspension estimation, and the designs of the particle removal and non-contact sampling devices. The assumptions about the particle morphology, contact area, and other adhesion properties are not necessary; the experimental removal data can be used for device design based on the threshold values of $\tau_w$. The approach can be used to analyze the effects of relative humidity[34-36] and electrostatic forces[37-39] in particle detachment, which has not been possible using AFM measurements.

The aerodynamic measurement method is susceptible to the surface and the particle roughness parameters: at the inception of the rolling motion, the particle may need to overcome the effect of asperities on the test surface or the particle surface. While smooth surface assumptions are used in this study, the sensitivity to the microscopic geometry at the particle surface interface allows for the study the surface roughness effects and particle morphology in rolling detachment scenarios.

The use of the CFD provides the calculation of forces acting on the particle in the boundary layer. The CFD allows for the estimation of the $\tau_w$, aiding in the design of experiments for any particle size morphology and orientation on the surface. While there are empirical relations that can yield the forces acting a particle in a boundary layer, the CFD, however, allows for the precise calculation of aerodynamic forces without the limiting assumptions of particle size, shape, and orientation, as well as the thinness of the boundary layer.

In our previous study[24], we characterized the adhesion forces acting on the particle. The adhesion forces depend on environmental conditions, sample preparation procedures, particles, and surface properties. Due to the significant variation in adhesion forces, it is necessary to gather a significant statistical data set. In AFM, the measurements are taken one particle at a time[19, 21, 40], limiting the expedient collection of large datasets. Our current setup provides up to 50,000 data points (particle removal events) in a single experiment, making the aerodynamic method cost effective.

## 5.3 Future Work

Our future work will include the application of the methods over a range of parameters and comparisons to the findings previously reported in the literature: relative humidity (RH=0-100%) [35], electrostatic force, particle aging (deformation) on the surface, and surface properties [41-43]. The method's sensitivity to microscopic geometry makes it an appropriate tool to study the microscale effect at the particle surface interface in the rolling detachment mechanism. Of interest is the extension of to study other threats like C4 and PETN which behave different with the surface owing to their different morphology.

The limitation of this study is in the particle size and the ability to interrogate relatively low adhesion forces, due to the assumption that the particles need to be contained within the viscous sublayer

(D<y+=5) and that the flow is fully developed where particle removal is measured. However, if the turbulent boundary layer is resolved, stronger adhesion forces can be evaluated. The shear stresses presented in this work are relatively low due to the low adhesion force between the silica particles and glass surface. In many real-world applications, the shear stress required to remove the particles from the surface is significantly higher than can be achieved in the flow cell. Other fluid dynamic systems can be used to study the particle adhesion force if the relationship between the flow and shear stress can be quantified. For example, particle detachment by the impinging jet has been previously studied [44-50]; the shear stresses in the impinging jets systems can be as high as 2kPa [51] compared to the 2-8 Pa range used in this work. A combination of shear stress calculations and particle removal data in the impinging jet system can extend the application of the method to higher adhesion force systems.

# References


1. Pumera, M.; Ambrosi, A., Trac-Trend Anal Chem. 2010, 29, 954–965; b) A. Bonanni, AH Loo, M. Pumera. *Trac-Trend Anal Chem* **2012,** *37*, 12-21.

2. Marshall, M.; Oxley, J. C., *Aspects of explosives detection*. Elsevier: 2011.

3. Keedy, R.; Dengler, E.; Ariessohn, P.; Novosselov, I.; Aliseda, A., Removal rates of explosive particles from a surface by impingement of a gas jet. *Aerosol Science and Technology* **2012,** *46* (2), 148-155.

4. Phares, D. J.; Holt, J. K.; Smedley, G. T.; Flagan, R. C., Method for characterization of adhesion properties of trace explosives in fingerprints and fingerprint simulations. *Journal of Forensic Sciences* **2000,** *45* (4), 774-784.

5. Zhan, X.; Fillingham, P.; Novosselov, I. V., Describing Micro-particle adhesion force using aerodynamic removal from surface. Aerosol science and technology: 2017.

6. Fletcher, R.; Briggs, N.; Ferguson, E.; Gillen, G., Measurements of Air Jet Removal Efficiencies of Spherical Particles from Cloth and Planar Surfaces. *Aerosol Science and Technology* **2008,** *42* (12), 1052-1061.

7. Verkouteren, J. R., Particle characteristics of trace high explosives: RDX and PETN. *Journal of forensic sciences* **2007,** *52* (2), 335-340.

8. Fletcher, R. A.; Brazin, J. A.; Staymates, M. E.; Benner, B. A.; Gillen, J. G., Fabrication of polymer microsphere particle standards containing trace explosives using an oil/ water emulsion solvent extraction piezoelectric printing process. *Talanta* **2008,** *76* (4), 949-955.

9. McFarland, A. R.; Ortiz, C. A.; Bertch Jr, R. W., A 10 μm Outpoint size selective inlet for Hi-Vol Samplers. *Journal of the Air Pollution Control Association* **1984,** *34* (5), 544-547.

10. Marshall, I.; Mitchell, J.; Griffiths, W., The behaviour of regular-shaped non-spherical particles in a TSI aerodynamic particle sizer. *Journal of Aerosol Science* **1991,** *22* (1), 73-89.

11. Chamberlain, R. T., Dry transfer method for the preparation of explosives test samples. Google Patents: 2002.

12. Bhattacharya, S.; Mittal, K. L., Mechanics of removing glass particulates from a solid surface. *Surface Technology* **1978,** *7* (5), 413-425.

13. Verkouteren, J. R.; Ritchie, N. W. M.; Gillen, G., Use of force-sensing array films to improve surface wipe sampling. *Environ. Sci.: Processes Impacts* **2013,** *15* (2), 373-380.

14. Tung, Y. S.; Mu, R.; Ueda, A.; Henderson, D. O.; Curby, W. A.; Mercado, A., The Study of Sublimation Rates and Nucleation and Growth of TNT and Petn on Slica and Graphite Surfaces by Optical and Atomic Force Microscopy and Ellipsometry. In *Atomic Force Microscopy/Scanning Tunneling Microscopy 3*, Cohen, S. H.; Lightbody, M. L., Eds. Springer US: Boston, MA, 2002; pp 135-152.

15. Chaffee-Cipich, M. N.; Sturtevant, B. D.; Beaudoin, S. P., Adhesion of explosives. *Analytical chemistry* **2013,** *85* (11), 5358.

16. Manrique-Bastidas, C. A.; Castillo-Chara, J.; Mina, N.; Castro, M. E.; Hernandez-Rivera, S. P., Nucleation and crystalization studies: a vibrational- spectroscopy investigation of 2,4,6- TNT. 2004; Vol. 5415, pp 1345-1356.

17. Yu, H.; Becker, T.; Nic Daeid, N.; Lewis, S., Fundamental studies of the adhesion of explosives to textile and non-textile surfaces. *Forensic Science International (Online)* **2017,** *273*, 88-95.

18. Derjaguin, B. V.; Muller, V. M.; Toporov, Y. P., Effect of contact deformations on the adhesion of particles. *Journal of Colloid And Interface Science* **1975,** *53* (2), 314-326.

19. Xu, X.; Mares, J.; Groven, L. J.; Son, S. F.; Reifenberger, R. G.; Raman, A., Nanoscale Characterization of Mock Explosive Materials Using Advanced Atomic Force Microscopy Methods. *Journal of Energetic Materials* **2015,** *33* (1), 51-65.

20. Zakon, Y.; Lemcoff, N. G.; Marmur, A.; Zeiri, Y., Adhesion of Standard Explosive Particles to Model Surfaces. *J. Phys. Chem. C* **2012,** *116* (43), 22815-22822.

21. Oxley, J. C.; Smith, J. L.; Kagan, G. L.; Zhang, G.; Swanson, D. S., Energetic Material/ Polymer Interaction Studied by Atomic Force Microscopy. *Propellants, Explosives, Pyrotechnics* **2016,** *41* (4), 623-628.

22. Bowen, R. C.; Demejo, L. P.; Rimai, D. S., A Method of Determining the Contact Area Between a Particle and Substrate Using Scanning Electron Microscopy. *The Journal of Adhesion* **1995,** *51* (1-4), 191-199.

23. Mills, O. P.; Rose, W. I., Shape and surface area measurements using scanning electron microscope stereo- pair images of volcanic ash particles. *Geosphere* **2010,** *6* (6), 805-811.

24. Zhan, X.; Fillingham, P.; Novosselov, I. V., Characterization of Adhesion Force in Aerodynamic Particle Resuspension. Kottapalli, K., Ed. Langmuir: 2017.

25. Bardina, J. E., Turbulence modeling validation, testing, and development. Huang, P. G.; Coakley, T. J.; Ames Research, C., Eds. Moffett Field, Calif. : National Aeronautics and Space Administration, Ames Research Center ; Springfield, Va. : National Technical Information Service, distributor: Moffett Field, Calif. : [Springfield, Va.], 1997.

26. Menter, F. R., Zonal Two Equation Kappa-Omega Turbulence Models for Aerodynamic Flows - NASA-TM-111629. Sponsoring Organization: NASA Ames Research Center: 1993.

27. Liu, Y.-H.; Maruyama, H.; Matsusaka, S., Effect of Particle Impact on Surface Cleaning Using Dry Ice Jet. *Aerosol Science and Technology* **2011,** *45* (12), 1519-1527.

28. Novosselov, I. V.; Ariessohn, P. C.; Dengler, E. D.; Hickner, M., Particle interrogation devices and methods. Google Patents: 2013.

29. Novosselov, I. V.; Ariessohn, P. C.; Dengler, E. D.; Hickner, M., Particle interrogation devices and methods. Google Patents: 2012.

30. Kottapalli, K.; Novosselov, I. V., Re-entrainment of fine particles from flat surfaces using inclined pulsed jets. Aerosol science and technology, 2017.

31. Darby, J. L.; Lawler, D. F., Ripening in depth filtration: effect of particle size on removal and head loss. Environmental Science and Technology: 1990; Vol. 24, pp 1069-079.

32. Y. Al-Otoom, A., Prediction of the collection efficiency, the porosity, and the pressure drop across filter cakes in particulate air filtration. Atmospheric Environment: 2004; pp 51-57.

33. Stern, S. C.; Zeller., H. W.; Schekman, A. I., The aerosol efficiency and pressure drop of a fibrous filter at reduced pressures. *Journal of Colloid Science* 1960; Vol. 15, pp 546-62.

34. Corn, M.; Stein, F., Re- entrainment of Particles from a Plane Surface. *American Industrial Hygiene Association Journal* **1965,** *26* (4), 325-336.

35. Gotoh, K.; Takebe, S.; Masuda, H.; Banba, Y., The Effect of Humidity on the Removal of Fine Particles on a Solid Surface using High- speed Air Jet. *KONA Powder and Particle Journal* **1995,** *13*, 191-203.

36. Ibrahim, A. H.; Dunn, P. F.; Brach, R. M., Microparticle detachment from surfaces exposed to turbulent air flow: Effects of flow and particle deposition characteristics. *Journal of Aerosol Science* **2004,** *35* (7), 805-821.

37. Boumsellek, S.; Alajajian, S.; Chutjian, A., Negative- Ion formation in the explosives RDX, PETN, and TNT by using the reversal electron attachment detection technique. *Journal of the American Society for Mass Spectrometry* **1992,** *3* (3), 243-247.

38. Farnoosh, N.; Adamiak, K.; Castle, G. S. P., Numerical calculations of submicron particle removal in a spike-plate electrostatic precipitator. *Dielectrics and Electrical Insulation, IEEE Transactions on* **2011,** *18* (5).

39. Ranade, M. B., Adhesion and Removal of Fine Particles on Surfaces. *Aerosol Science and Technology* **1987,** *7* (2), 161-176.

40. Esayanur, M. S.; Yeruva, S. B.; Rabinovich, Y. I.; Moudgil, B. M., Interaction force measurements using atomic force microscopy for characterization and control of adhesion, dispersion and lubrication in particulate systems. *Journal of Adhesion Science and Technology* **2005,** *19* (8), 611-626.

41. Soltani, M.; Ahmadi, G., Particle Detachment from Rough Surfaces in Turbulent Flows. *The Journal of Adhesion* **1995,** *51* (1-4), 105-123.

42. Henry, C.; Minier, J.-P., Progress in particle resuspension from rough surfaces by turbulent flows. *Progress in Energy and Combustion Science* **2014,** *45*, 1-53.

43. Mizes, H.; Ott, M.; Eklund, E.; Hays, D., Small particle adhesion: measurement and control. *Colloids and Surfaces A: Physicochemical and Engineering Aspects* **2000,** *165* (1), 11-23.

44. Masuda, H.; Gotoh, K.; Fukada, H.; Banba, Y., The removal of particles from flat surfaces using a high- speed air jet. *Advanced Powder Technology* **1994,** *5* (2), 205-217.

45. Smedley, G. T.; Phares, D. J.; Flagan, R. C., Entrainment of fine particles from surfaces by gas jets impinging at normal incidence. *Experiments in Fluids* **1999,** *26* (4), 324-334.

46. Phares, D. J.; Smedley, G. T.; Flagan, R. C., The wall shear stress produced by the normal impingement of a jet on a flat surface. *Journal of Fluid Mechanics* **2000,** *418*, 351-375.

47. Otani, Y.; Emi, H.; Morizane, T.; Mori, J., Removal of fine particles from wafer surface by pulse air jets. *Kagaku Kogaku Ronbunshu* **1993,** *19* (1), 114-119.

48. Otani, Y.; Namiki, N.; Emi, H., Removal of Fine Particles from Smooth Flat Surfaces by Consecutive Pulse Air Jets. *Aerosol Science and Technology* **1995,** *23* (4), 665-673.

49. Ziskind, G.; Yarin, L. P.; Peles, S.; Gutfinger, C., Experimental Investigation of Particle Removal from Surfaces by Pulsed Air Jets. *Aerosol Science and Technology* **2002,** *36* (5), 652-659.

50. Smedley, G. T.; Phares, D. J.; Flagan, R. C., Entrainment of fine particles from surfaces by impinging shock waves. *Experiments in Fluids* **1999,** *26* (1), 116-125.

51. Fillingham, P.; Murali, H.; Novosselov, I. V., Non-Dimensional Parameter for Characterization of Wall Shear Stress from Underexpanded Axisymmetric Impinging Jets. Journal of Fluid Engineering: ASME (in print), 2017.

# **Appendix A:** Equivalent Diameter of a Particle

Particle size, in a sense commonly used, is a linear length measure, measured in SI unit [m]. In this sense, it can be uniquely defined only for spheres, where it is the diameter (or radius). For all other shapes, the particle size must be defined via the measuring procedure. So-called derived diameters are determined by measuring a size-dependent property of the particle and relating it to a single linear dimension. The most widely used of these are the equivalent diameters, is the equivalent spherical diameters.

Important equivalent diameters are:

a) Volume-equivalent sphere diameter ($D_{volume}$)

Volume-equivalent sphere diameter is the diameter of a sphere with the same volume as the particle ($V_{particle}$).

$$D_{volume} = \left(\frac{6}{\pi} V_{particle}\right)^{1/3}$$

b) Surface-equivalent sphere diameter ($D_{surface}$)

Surface-equivalent sphere diameter is the diameter of a sphere with the same surface as the particle ($S_{particle}$).

$$D_{surface} = \left(\frac{6}{\pi} S_{particle}\right)^{1/2}$$

c) Stokes diameter ($D_S$)

Stokes diameter is the equivalent diameter corresponding to the diameter of a sphere with the same final settling velocity as the particle undergoing laminar flow in a fluid of the same density and viscosity), defined via the Stokes relation,

$$D_s = \sqrt{\frac{18\eta v}{(\rho_S - \rho_L)g}}$$

Where,

$\eta$ is the viscosity, $\rho_s$ is the density of the solid particles, $\rho_L$ is the density of pure liquid, $g$ is the gravitational acceleration, and, $v$ is the final settling velocity.

d) Hydrodynamic equivalent diameter ($D_H$)

Hydrodynamic equivalent diameter is the diameter of a sphere with the same translational diffusion coefficient ($D_{translation}$) as the particle in the same fluid under the same conditions, defined via the Stokes-Einstein relation,

$$D_H = \frac{kT}{3\pi\eta D_{translational}}$$

Where,

$k$ is the Boltzmann constant, T is the absolute temperature and $\eta$ is the viscosity of the liquid medium.

e) Sieve diameter ($D_{sieve}$)

Sieve diameter is the equivalent diameter corresponding to the diameter of a sphere passing through a sieve of defined mesh size with square or circular apertures.

f) Projected area diameter ($D_P$)

Projected area diameter is the equivalent diameter corresponding to the diameter of a sphere or circle with the same projected area as the particle. In general, $D_P$, is orientation-dependent, particularly for an isometric particles. The equivalent area diameter measured via microscopic image analysis, $D_M$, usually refers to preferential (non-random) 'stable' orientation and thus is not the same as $D_P$ for random orientation; another equivalent area diameter, conceptually analogous to the projected area diameter, is the random section area diameter, which can be measured from random cuts (planar sections, polished sections) via image analysis

The image analysis Software is based on a neural scheme which improves the functionality of computation every time you use it in a set. The area factor was modified, and the equivalent size of the particle is larger than the theoretical value as shown in Figure A 1.

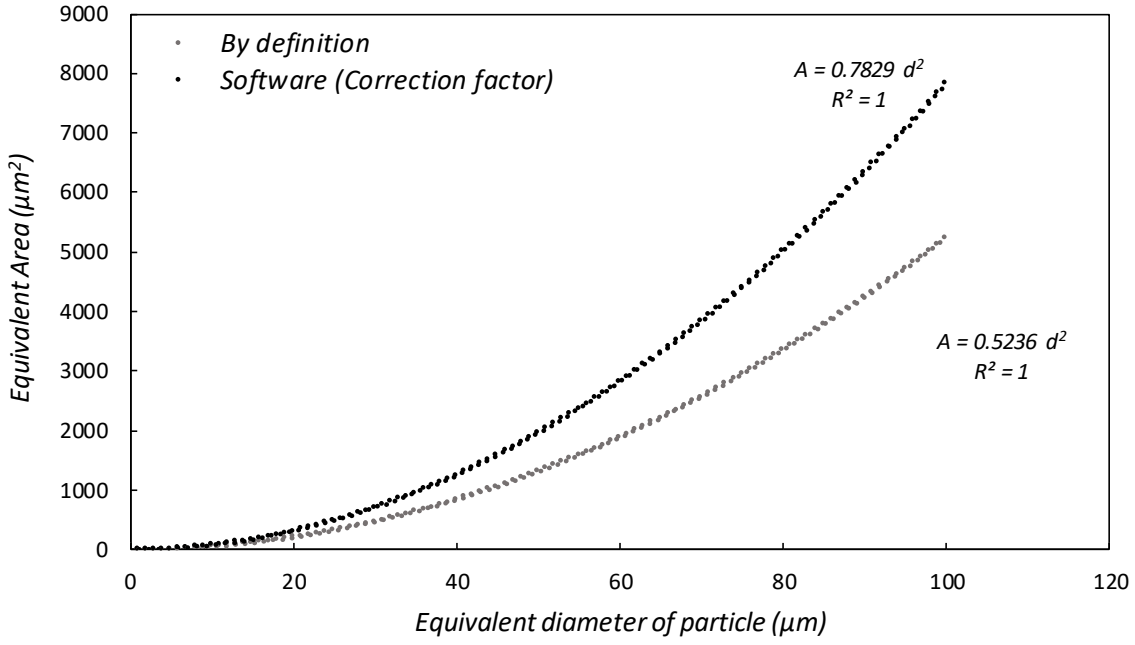


Figure A 1 *The difference in the theoretical and actual computed equivalent diameter of the particle.*

# **Appendix B**: Detection of Trace Residues on Metal Fiber Mesh using IMS

The capture potential and detection limits with a direct spike of particulate trace residues was investigated. Solutions of 3 trace explosives, RDX, TNT, and DNT were created from 0.1ng/µl to 1000 ng/µl. All the solutions were created, and 1 µl of each solution was loaded to the 2 X 2-inch metal fiber mesh and were tested for detection. 20 experiments were done at each concentration for each trace explosive. The solutions were precisely loaded with the help on precision micro syringes. The goal of this study was to see the capture capability of the metal fiber mesh.

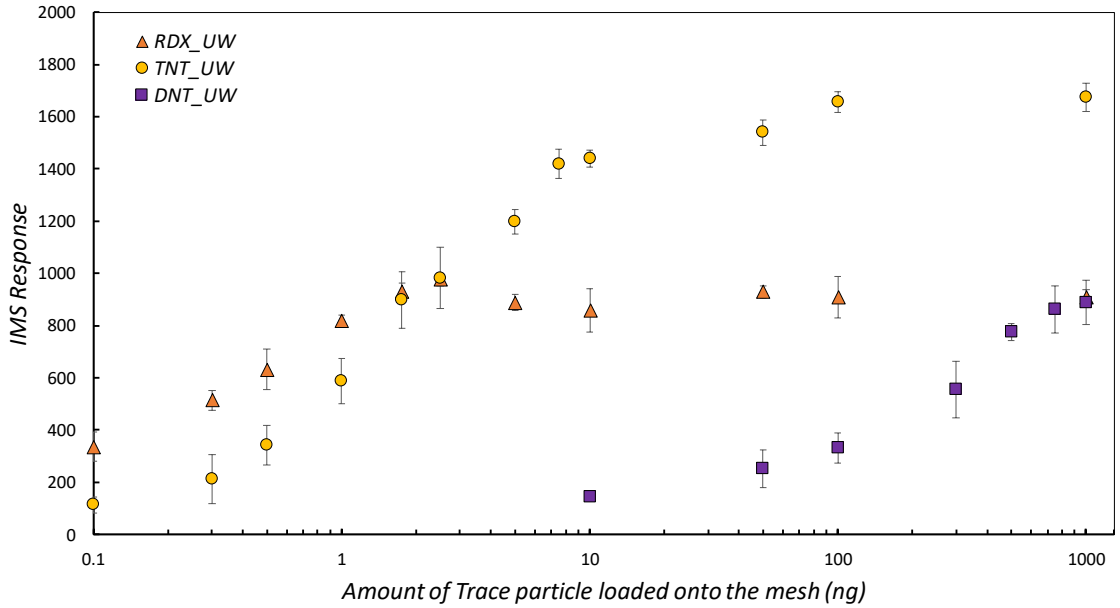


**Figure A 2** *IMS reading from direct spike deposition on the metal fiber mesh of 60-micron porosity.*

Different porosities of Metal fiber mesh were tried, and following conclusions were made

As filter cutoff porosity falls:

- ✓ Capture efficiency improves
- ✓ Backpressure increases
- ✓ Operational lifetimes decrease
- ✓ IMS signal is reduced